EXPERIMENTAL INVESTIGATION OF SPHERE SLAMMING TO QUIESCENT

WATER SURFACE-PRESSURE DISTRIBUTION AND JETTING FLOW FIELD

A Thesis

by

WAN-YI WEI

Submitted to the Office of Graduate and Professional Studies of
Texas A&M University
in partial fulfillment of the requirements for the degree of

MASTER OF SCIENCE

Chair of Committee,	Kuang-An Chang
Committee Members,	David Brooks
	Stefan Hurlebaus
	Jun Zhang
Head of Department,	Robin Autenrieth

December 2014

Major Subject: Ocean Engineering

ABSTRACT

Sphere slamming pressures and corresponding jetting flow fields were studied in an experimental approach. Correlations between sphere impacting forces and jetting flow occurrences were explored. Pressure sensor was used to investigate the slamming pressures distributed around the sphere at five measuring points. The jetting flow fields were carried out using the bubble image velocimetry (BIV) technique. Time series jetting flow speeds were successfully examined. The pressures and jetting were studied in four various sphere impacting speeds as four cases. Five designed impacting angles which means impacting measuring point around sphere surface for sensor were conducted for each case. Maximum pressures happened at impacting measuring point of 0°. Maximum jetting flow speed traveled as the front of jetting fields. The pressures and jetting speeds was proportional to corresponding impacting speed. Control volume approach was suggested to examine the force transfer between slamming and jetting. The jetting forces were compared with the impacting forces with respect to increasing surface area of sphere under water. The jetting forces detected after maximum jetting speed were similar with the impacting forces. The jetting flow velocities were able to be estimated. Maximum evaluated jetting flow velocity happened immediately after slamming occurred.

DEDICATION

To

My family

Father and Mother

My husband

Brother

My pet Brownie

I would have never had today's achievement without your selfless support

ACKNOWLEDGEMENTS

TABLE OF CONTENTS

LIST OF FIGURES

LIST OF TABLES

CHAPTER I

INTRODUCTION

Wave slamming is a major concern of damaging marine structures not only for the moving type structures like ships and vessels but also for offshore structures which are located in the fixed locations such as platforms and wind turbines.

When ships and vessels travel in the ocean, bottom slamming happened of structure is a common situation resulting from ships suddenly plunged into the sea water. The highly impulsive pressure is produced in the structure of ships in a short period of time that is generally less than 1 second. A heavy slamming situation happened the structure bottom may lead severe damages of structure.

Meanwhile, the fixed type offshore structures are easily acquired to highly intensive pressures caused from wave breaking of sea water impacting or from significant wave height during storm seasons. Highly concentrated pressures acting at local spots located on the wetted surface of structures are predictable risks and may reduce the lifetime of marine structures. About slamming in marine applications, Faltinsen et al. (2004) summarized three phases of slamming: water entry on initially calm free surface, wet deck slamming, and green water and sloshing. Investigation of bottom slamming issue for the interaction of two-phase flows including air and liquid which can provide significant loads to marine structures is worth to explore.

Experimental investigations were studied by research groups to examine correlations between object impacting speed and its corresponding impacting pressures.

An important concern of the experiments is to measure water loads on the structures and further verify mathematical results with various designed impacting speed. In order to simulate behaviors of marine structures, designed experimental objects are chosen as similar as real marine structures. Even shapes of marine structures are more complex and not as a simple geometry, several representative shapes of important elements for the marine structures are still valuable to be investigated.

Flat panels are a kind of common shape of offshore structures like wetted decks and hull of operating tugs or barges. Huera-Huarte et al. (2011) commenced the study for water loads on panels. They focused to examine the slamming forces on the plates as the marine structures encountered water impacting. The Slingshot Impact Testing System (SITS) was used to allow the objects falling on the free water surface with several designed angles and speeds. A special trapped air phenomenon between the plate and the water surface was found with the deadrise angles less than 5°. They concluded that air cushion reduced the impacting force since the measured pressures are always smaller than the asymptotic theory. Furthermore, the measured results were not affected by the trapped air and had significant correlation with the asymptotic theory when the deadrise angles are larger than 5°.

Cylindrical structures also play an important role in the offshore industry. Some drilling platforms are constructed by the cylindrical elements. Van Nuffel et al. (2013) studied local hydrodynamic loads on surface of a quasi-rigid cylinder in experimental approach. They conducted the cylinder dropping experiment that a cylinder sphere object dropped from the predetermined height to the quiescent water surface as the wave

slamming on the naval structures. Experimental results were compared with the Wagner theory. It was found that the experimental results agreed with estimations in theory when the deadrise angles were larger than 4.25^{o} if the theoretical results were averaged over the surface of pressure sensor. Otherwise, the estimations by theory are too high to predict their experimental results.

In addition to flat panels and cylinder structures, axisymmetric bodies are one of common structure models for testing sea loads on the marine structures. Experimental axisymmetric model tests not only simulate wave slamming on the marine structures that are truss or connection points of jackets but also can be applied on the wave energy converters as point absorbers. De Backer et al. (2009) conducted a series of experiments of bottom slamming in three types of axisymmetric objects: hemisphere and two types of conical shapes. The axisymmetric bodies were tested with different designed angles from a specific height and the measured experimental pressures were compared with the analytical theory. Generally, the differences between experimental peak pressures and analytical peak pressures in three types of experimental objects are around 25%~50%.

Moghisi et al. (1981) started to investigate the initial forces on a sphere slamming to a quiescent water surface. Their experimental tests are as a harbinger for studying the force of sphere slamming. Even today, it valuably provides the insightful information for wave slamming.

Even impacting loads on the structures were already studied through well-planned experiments. After slamming occurring, the second time damages caused from jetting and splashes were another relative topic for the examination. Meanwhile,

examining flow field of the slamming phenomena is the first step to study the energy

transfer from impacting to the water pool. Lin et al. (1997) examined not only slamming

forces acted on cylinder and compared the results with the Wagner's theory but also

acquired flow fields of water pool for further investigating of corresponding water

velocity. It is valuable that acquired slamming pressures were combined with an

experimental image. However, some physical properties of jetting flow like jetting

speeds and motion directions are important for comprehending the momentum transfer

from impacting forces to the jetting flows.

Numerous numerical models for studying hydrodynamic impacts and digging the

jetting phenomena were already developed widespread. Battistin et al. (2003) presented

a numerical simulation with the fully nonlinear boundary-element method to investigate

the arbitrary shape of 2-dimensional symmetric bodies and axisymmetric bodies which

impacted free water surface. There are two principal assumptions that are potential flow

with an incompressible fluid and neglecting surface tension and gravity. This application

of nonlinear boundary element method is capable to simulate jetting flow caused from

the impacting.

Gu et al. (2014) developed a numerical model based on the Navier-stokes

equations (NSE) with a two-fluid free surface approach. The results about impacting

forces and surface pressure distributions were verified by experimental tests and other

numerical tests for the vertical entry problems. And later the free surface solver is able

to apply for both vertical entry and oblique entry issues. Their model was

well-developed to simulate the impacting situations for both obtaining impacting forces

and distribution of pressure around the wet surfaces and relative entire flow field. Nevertheless, the characteristic of jetting was still not presented especially in the case of sphere slamming simulation.

Abraham et al. (2014) also provided a mathematical model to simulate the experiences of sphere as the expendable bathythermograph (XBT) entry water. They would like to provide a reliable method to simulate the sphere slamming issue. They concluded the drag coefficient derived from numerical tests was independent on some parametric variations such as sphere impacting speed, surface tension and Re numbers etc. They provided a series of clear jetting patterns around sphere at several time frames during slamming occurred although the detailed information was still not included.

The sphere slamming issue was also simulated using the Smooth Particle Hydrodynamics (SPH) approach mentioned by Maruzewski et al. (2010). The objective of their work was to show the ability of SPH to simulate complex 3-dimensional problems. Their results including time-series pressures and impacting forces were compared with the experimental results. The result of numerical simulation was close to the experimental data. They also provided images of jetting spilling out during various water entry stages, in which the images included more details about jetting impact but lacked for offering information of the momentum transfer from impacting to the pool and then to the jetting.

Experimental tests, observing the motion of jetting flow resulted from solid sphere slamming, were studied by Thoroddsen et al. (2004). They were able to gain a series of experimental jetting images using a novel-high-speed video camera. They

found that the jetting emerged almost immediately after the slamming occurrence, and concluded that the speeds of jetting are related to the Re number. When the Re number $>2\times10^4$, the speeds of jetting were almost 30 times of the vertical sphere impacting velocity. The jetting growth was anticipated from the moment that spheres initially contacted water surface to the stage which the jetting spilled out with high speeds through the horizontal direction. The added mass approach was applied to figure out the ratio of absorbed energy between jetting and pool from impacting. The impacting energy transported to jetting was about 90 %. However, the flow field for measuring jetting flow speeds was lack to acquire impacting forces.

Yoon et al. (2007) investigated physical aspects of splashing caused from water drops in an experimental approach. They regulated the relationship of drop impact speed and the corresponding ejection speed, and traced the velocities of several ejected water particles during short time period. Nevertheless, the whole ejected flow field velocity which is important to examine the energy transfer was not obtained.

The primary goal of the study is to evaluate a physical correlation between the impacting forces and the jetting flow fields for further understanding the transfer of energy from slamming to the emerged jetting. There are two main parts included: the acquisition of slamming pressure and the measurement of jetting flow fields.

Bubble image velocimetry (BIV), a technique using bubbles as tracers to capture the velocity of bubble, is introduced to obtain the slamming jetting flow fields. Ryu et al. (2005) developed BIV that is a method modified from the concepts of PIV and combined with velocity field built by tracing the difference of gray scales between the interface of

air and water. This approach is suitable for measuring the multiphase flow fields. Ryu et al. (2007) applied BIV to measuring the 2-dimensional green water over a structure. 3-dimensional green water flow over a deck shape structure was detected by BIV technique (Chang et al., 2011). Recently, BIV was successfully applied to investigate in liquid sloshing issue by Song et al. (2013). BIV is proven as a mature technique and able to acquire the velocities of whole flow filed with reliable accuracy. BIV is especially suitable to apply on the aerated flow like the impacting situation of slamming issues.

To figure out the momentum transfer from slamming impacting forces to the corresponding emerged jetting flow is the major objective. The sphere slamming experimental tests were conducted in the indoor wave tank with four different impact conditions. Pressure sensor was mounted inside the sphere in order to obtain impacting forces in several different measuring locations for wet surface of the sphere. BIV was adopted to obtain not only the jetting flow fields but also to measure the corresponding sphere dropping speeds. The correlation of momentum transfer within the entire system was investigated to find out the jetting forces which may cause second time damages of marine structures. The details about experiments and analysis are explained as following chapters.

CHAPTER II

EXPERIMENTAL SET-UP

A series of experiments were conducted in the hydro lab at Texas A&M University in order to investigate momentum transfer of slamming using solid sphere suddenly impacting quiescent water surface. The wave tank located in the hydro lab was employed for the slamming experiment, and the dimension of wave tank is 36 m long × 0.9 m wide × 1.5 m deep. The wave tank is constructed with glass observation windows, in which clear images obtained without blocks and experimental process observed in time for further accurate analysis of flow field.

A solid sphere with hull structure for inserting pressure sensor is the main facility which is an approximation for cylindrical naval structures in order to study for bottom wave slamming or severe sea condition. The sphere with 6 inch external diameter and 1 inch thickness was made by plastics and held by a steel system which provides stable swaying motion to allow the sphere impacting water surface with different initial rising elevations. Four types of elevation were adopted to develop four impacting sphere speeds as table 1. The detail of tracing the speed of sphere will be explained in the later section of this chapter.

Table 1. Impacting velocity of X component and Z component for 4 cases

	horizontal Velocity (m/s)	Vertical Velocity (m/s)	Impacting Speed (m/s)	Impacting Angle (θ)
Case 1	1.04	0.82	1.32	51.75
Case 2	1.64	1.33	2.11	51.08
Case 3	2.54	2.21	3.37	49.08
Case 4	3.15	2.91	4.29	47.27

The center of the sphere is located in 0.45 m away from the both side wall of tank. The quiescent water depth is 0.65 m during the entire experimental process.

The steel system located at the top of wave tank is assembled firmly by the triangle supporting system in order to limit the structure damping. An electric magnitude is attached on the system to control the releasing moment of the sphere. The sphere is unattached by blocking electric loop of the electric magnitude and falls onto the water. The dimension of the entire steel system is as Fig. 1.
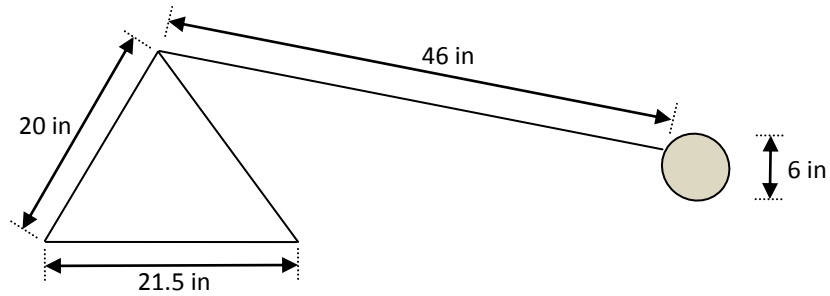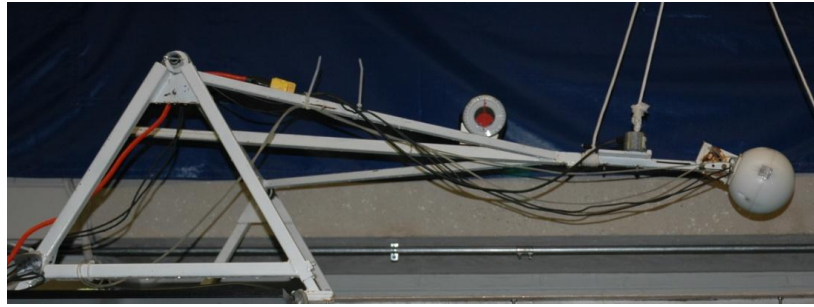
Figure 1. Experimental set-up.

The controls of sphere releasing, acquisition of pressure data and triggering high speed camera are synchronized by a National Instruments Lab VIEW program. The details of pressure measurements and BIV system are explained separately as following sections.

Pressure Measurement

Pressure sensor: A Kistler 4053A10 pressure sensor which is piezo-resistive relative design was used to measure the pressure response during the slamming experiment process. The range of pressure measurement of the pressure sensor is from 0 to 10 bar. The natural frequency of the sensor is larger than 50k Hz. Because of the high natural frequency of the pressure sensor, it is suitable in the dynamic measurements like slamming circumstance.

The pressure sensor was calibrated properly before slamming experiment commenced. The calibration demonstrates that there is a linear and stable relationship between response voltage and its reference pressure as Fig. 2.
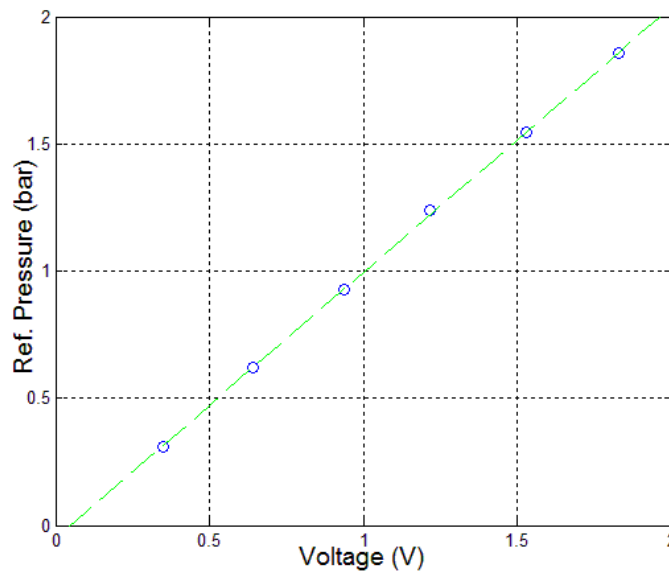
Figure 2. Calibration of pressure sensor.

Measuring positions: One pressure sensor was inserted inside the sphere with an ideal response surface. The surface of sensor and the surface of sphere are perfectly smooth and matched well without any rough and uneven condition. Five designed angles, shown in Fig. 3, were employed to explore the pressure distribution over the cylindrical structure surface during the bottom slamming occurred. The designed impacting angles of measurement are controlled manually by adjusting rotation systems to rotate the sphere to fit the desired angle between pressure sensor and immobile water surface. On the other hand, each experiment is conducted with one specific measuring angle and the pressure is measured in all process from initial sphere height to the sphere contacting the water surface, and behaviors of spheres under water. . In order to avoid the fluctuation of pressure measurement, the measurement at each impacting angle is repeated 20 times and the averaged pressure value was taken.

Sample rate selected and error estimated: The peak pressures exist immediately after slamming occurred; hence the small time interval is required for pressure sensor to gain precise peak values. Several slamming tests have been done with the same impacting sphere speed and different pressure sampling rate and the results are as table 2. Each experiment with different sample rate repeated 5 times. 50k Hz sample rate was accepted for detecting the peak pressure value. The natural frequency of the sensor is chosen as 50k Hz with the relative lower standard derivation, 0.029 bar, in which 50k Hz sample rate is sufficient to detect the peak pressure value with an accurate and steady characteristic.
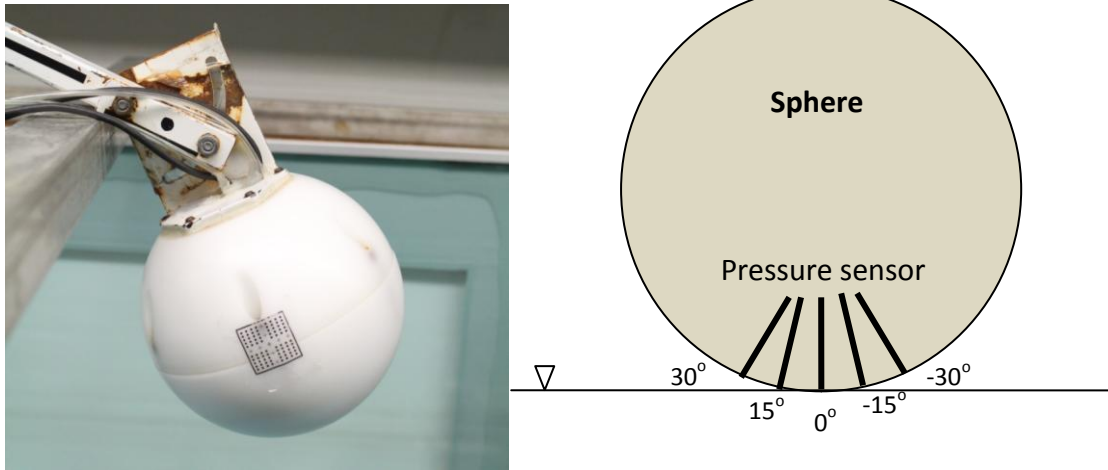
Figure 3. Impacting angles and sensor positions.

Table 2. Sampling rates vs. measured peak pressures

Sample rate (Hz)	Averaged peak pressure (bar)	Standard Deviation (bar)
20 k	1.59	0.045
50 k	1.63	0.029
100 k	1.60	0.114
200 k	1.66	0.071

BIV

High speed impacting from sphere to quiescent water surface causes water particles spilled out. This jetting flow situation happens along with impacting pressure detected. In order to understand the energy transfer, a measurement technique BIV, Ryu et al. (2005), was employed to gather the jetting flow speed.

Set-up: The experimental set-up for BIV is showed as Fig. 4. Laser facilities are not used for jetting flow measurement but back-lit lights are required for providing lightening sources. Meanwhile, a thin and white translucent acrylic plate was fixed in the back side of the tank in order to allow the back-lit light to be uniformly distributed. Because of the properties of grayscale varying with water and air in the experimental images, the technique of BIV is able to trace the velocity of jetting particles at each time frame.

Figure 4. Top view of experimental set-up.

High-speed camera: A high-speed camera (Phantom, Miro M140 / M340) was used to capture a series of experimental images for the analysis of BIV. The camera is capable to take 12000 frames per second (fps) with 1280×184 pixels of field of view, and the resolution is 0.256×0.0368 m^2. This designed field of view (FOV) is necessarily sufficient to obtain the jetting flow speed because the dimension of the sphere is 0.1524 m and the relatively high frame rate is helpful to collect the jetting speed.

Depth of field: The depth of field (DOF) is the main area where the jetting flow speed is measured since the leaser sheet is no longer required. The objects within the DOF are clear and focused but blurred if outside DOF. The DOF can be varied by adjusting the aperture of lens and the distance from camera to object. The lens used is Nikon 50 mm focal lens. The DOF is defined as $D = S - R$. Where S is the farthest focal limit $S = Lf^2/(f^2 - NLC_c)$, R is the nearest focal limit $R = Lf^2/(f^2 + NLC_c)$, L is the distance between the experimental object and camera, f is the focal length of camera, N is the f-number of aperture of camera and C_c is circle the confusion of the camera.

The relative parameters of DOF are listing the following: the DOF is 6.97 cm, the focal length of camera f is 50 mm), the circle of confusion C_c is 0.017 mm), the distance L is 1.13 m, and the aperture of lens is 4. R and S are calculated as 1.097 m and 1.167 m, respectively. According to the limitation of DOF, the water particles outside the plan become blurred. The 3.1 % of uncertainty of the jetting flow speed measurement is estimated as $D/2L$ (Ryu et al. 2005)

Jetting flow speed calculation: Commercial software for BIV calculation from La Vision Inc. was used to gain velocity vectors for jetting flow speed. The multi-pass iteration with cross-correlation was applied. The window size is initial 32×32 pixels and 16×16 pixels is the final window size with 50% overlapped adjacent window, in which 1 pixel equals to 0.2 mm for BIV analysis.

Before BIV calculation, algorithmic mask is applied by defining the outside grayscale range for water particles and air interface area in order to block unwanted area of experimental field of view. Each case repeated 20 times and the final velocity vectors are averaged. During this process, the spurious vectors are erased by setting a threshold: averaged values of vectors are only taken if over 16 vectors are repeatable.

The inverted images were converted by the software from raw experimental images. Since the water particles are as the brightest dots in the images, the BIV technique is able to compute the velocity filed for jetting by captured water particles but not work for the area where no water and air presented. The process of BIV to acquire the velocity field is illustrated in Fig. 5.
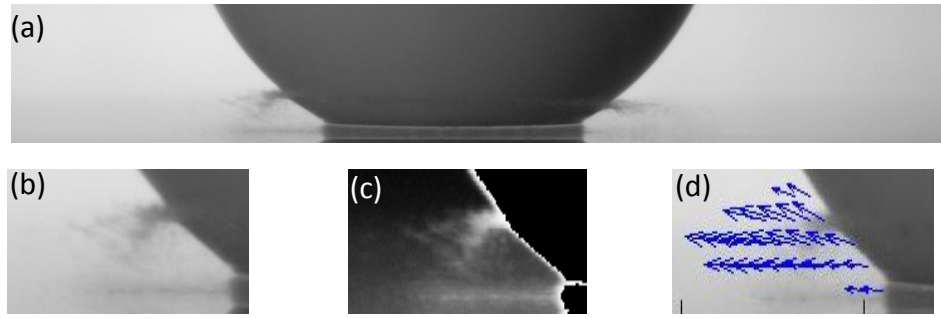
Figure 5. Procedures for jetting flow field calculation from BIV (a) Raw experimental image (b) close view of raw image (c) inverted image (d) BIV result.

Impacting Speed Acquisition

The BIV method was employed to trace impacting sphere speed. Artificial particles were attached on the surface of sphere for BIV uses. The measurements repeat 5 times for each case. Figure 7 shows the average sphere speed of case 4 which is the case with maximum impacting sphere speed. The standard error is around 0.04 (m/s) of the 5 repeated measurements. The average value of sphere speed of each case was taken for the further analysis. Notice that the speed is the combined information of vertical component and horizontal component velocity as table 1. Time equal to zero is defined as the moment of sphere firstly touched the quiet water surface. The impacting speeds of 4 cases are shown as the figure 6.
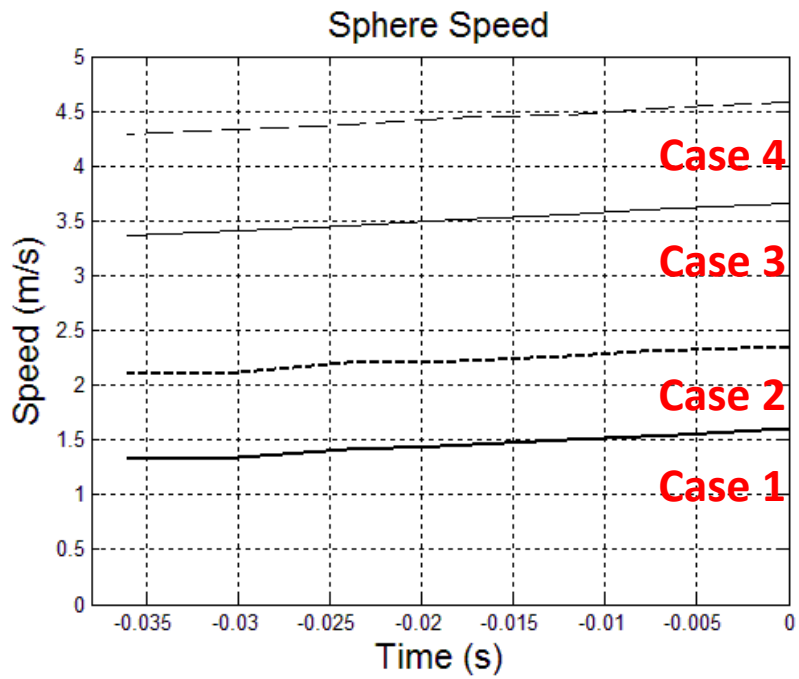
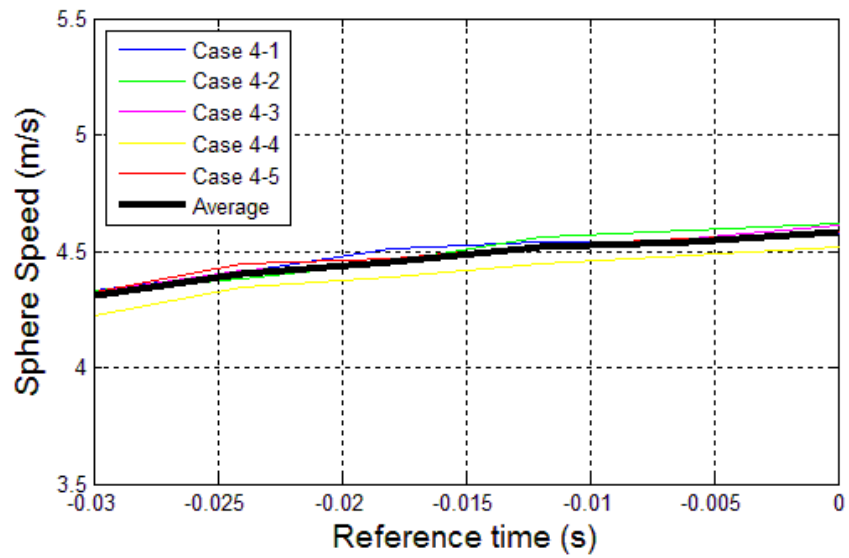**Figure 6.** Impacting sphere speeds of 4 cases.

Figure 7. Averaged sphere speed of case 4.

18

CHAPTER III

PRESSURE MEASUREMENT

Impacting pressure of bottom slamming situation is an issue of the safety of marine structures. The primary work of this chapter is to evaluate the peak and time-series pressures during the slamming situation occurred. One pressure sensor was used for pressure measurements. From chapter II, the range of pressure measurements covered is total 60° (30° ~ -30°) of the sphere surface including 5 measuring points. 4 different impacting velocities were developed to examine the slamming pressure.

Figure 8 Shows a tendency of the measured pressures from 0 to 0.002 seconds. Because of the limitation of figure drawing, there are only 10 repeated measurements plotted of case 4. The black line is the average pressure of 20 repeated measurements.
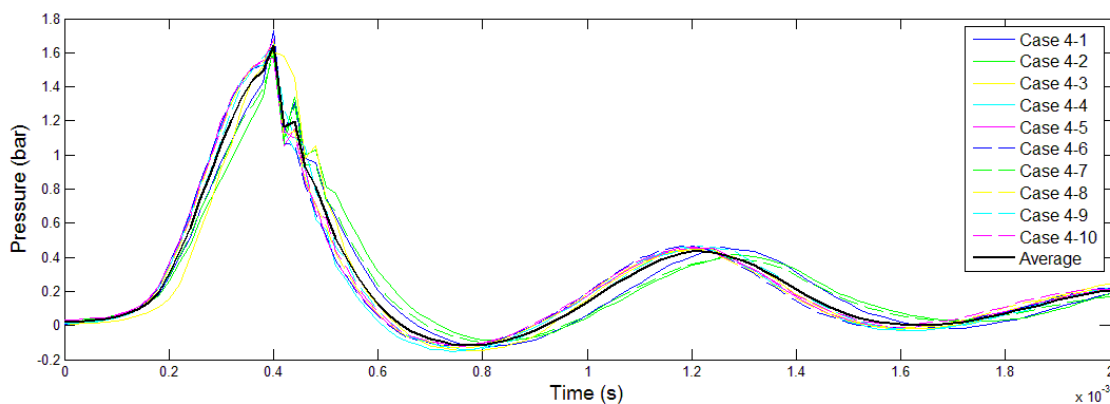

Figure 8. Time-series pressures of case 4.

The slamming impacting pressures have a reproducible characteristic; similar peak pressures and time-series tendencies are found with slight variations of each measurement at the same experimental conditions. The pressures shown in Fig. 8 were directly carried out by pressure sensor without removing offset at the impacting angle of 0°. There are different rising time scales between the first peak pressure and the second pressure values. The rising time of first peak pressure is less than 0.2 ms. De Backer et al. (2009) found the rising time of first peak is around 0.2 ms with about 7° deadrise angle, and the rising time of second peak pressure is around 0.4 ms which is twice of the first peak rising time.
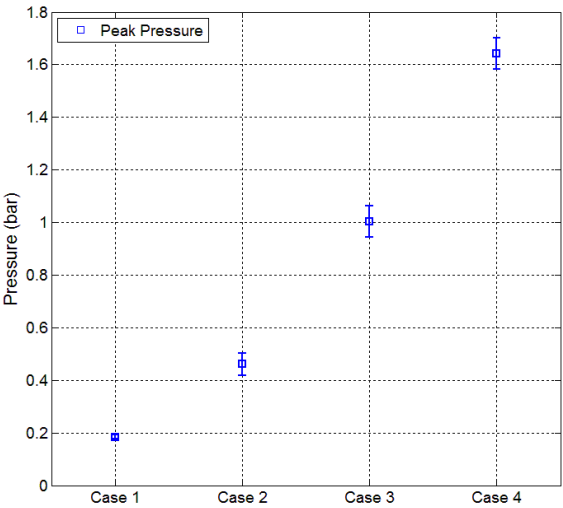

Figure 9. Mean peak pressures from 20 repeated measurements (0° deadrise angle) with standard deviations.

Figure 9 shows averaged peak pressures of each case in 20 repeatable experiments and their standard deviations. The standard deviations of the four cases are from case 1 to case 4: 0.007, 0.043, 0.059 and 0.059 bar, respectively. The standard deviation in all cases is around 6.2% $\pm$ 2.6% of the peak pressures. Based on the dynamic natural of slamming pressure, the range of pressure futuration is accaptable.

The time-series pressures are presented in Fig. 10. Through observing pressure maps, it is convenient to compare the pressure patterns which were measured in different deadrise angles. The time-series pressure records distinct tendencies between various angles. The data in a short period time of 0.02 are shown for each impacting angle around sphere surface as mentioned in the chapter II. The impacting angles from left-hand side to right-hand side in sequence of figure 3 are 30°, 15°, 0°, -15° and -30°. The sphere has a horizontal impact velocity in x-direction and a vertical impact velocity in z-direction because the sphere released as a sway motion by the electric magnitude. The x-direction motion is moved from right to left. The measuring points from the 30° ~ 0° were defined as the "identical zone". On the other hand, 0°~ -30° were defined as the "opposite zone".
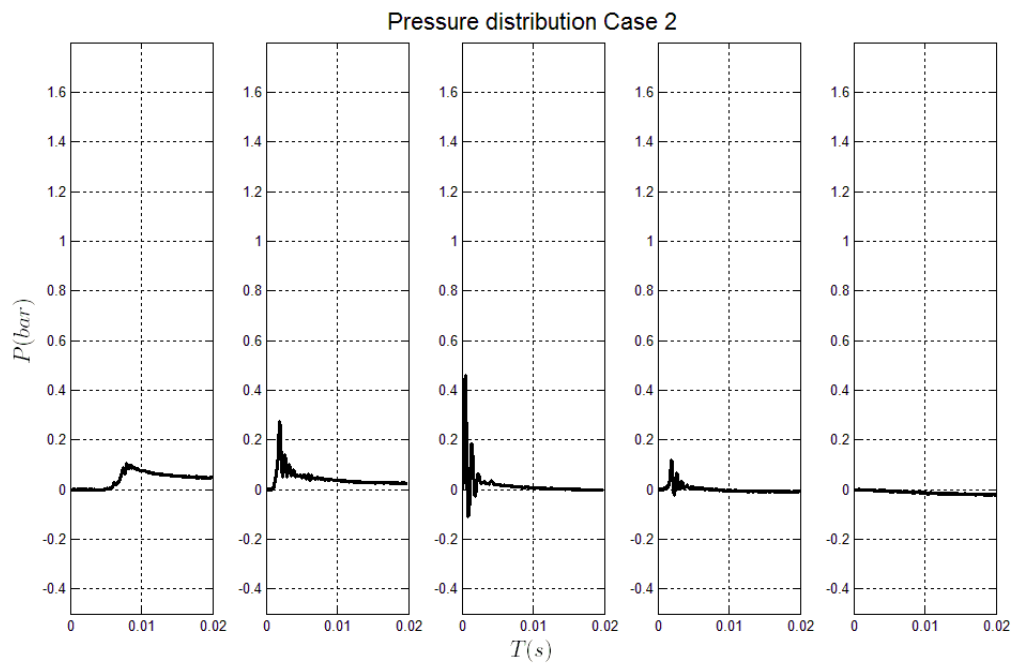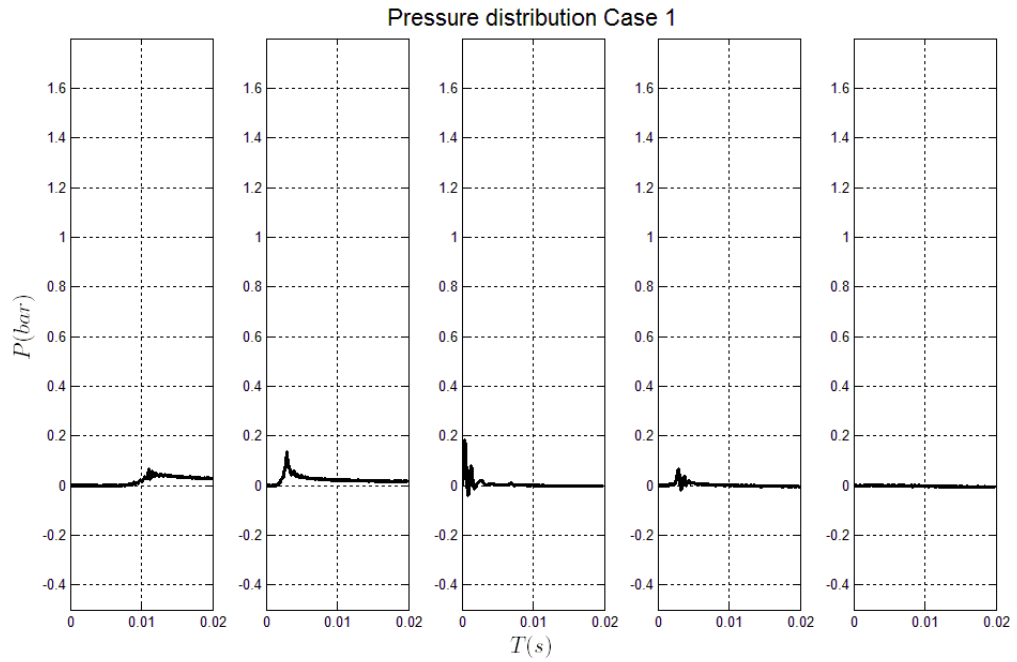
Figure 10. Time-series impacting pressure measurements for 4 cases with 5 measured impacting angles. 30°, 15°, 0°, -15° and -30° impacting angles are in sequence from left to right.

Pressure distribution Case 3
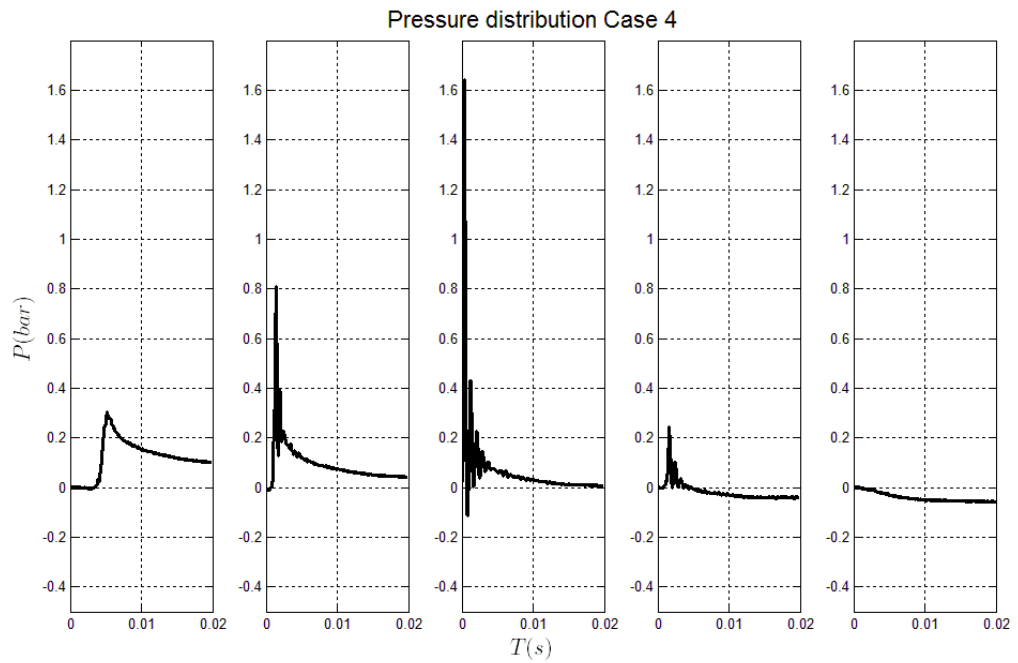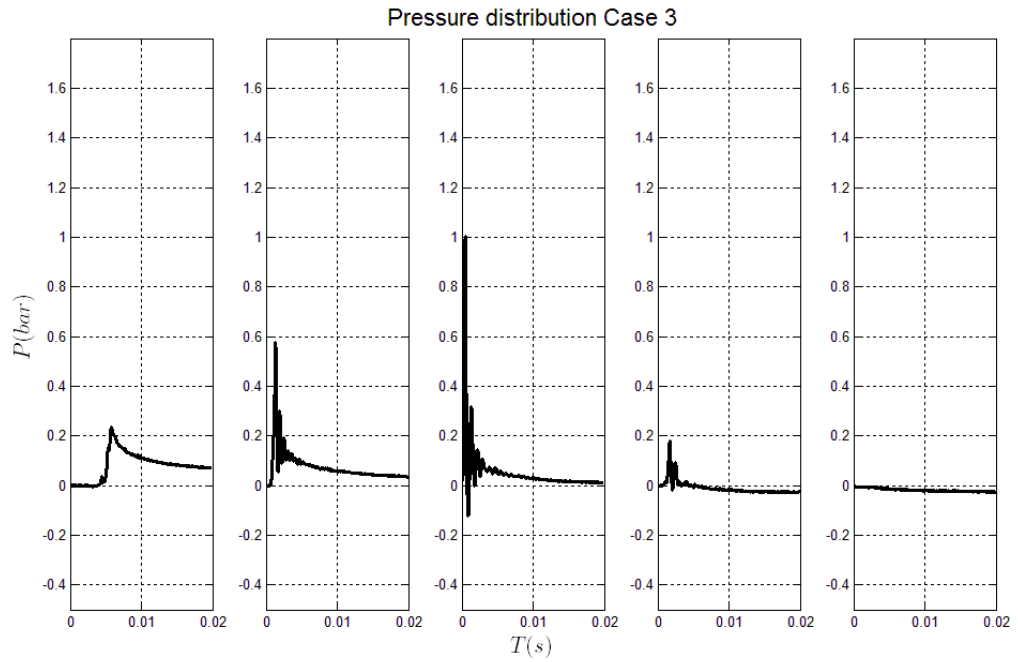
Pressure distribution Case 4

Figure 10. continued.

From the figure 10, the peak pressures increased though the higher impacting velocity for each 5 impacting angle. The peak pressures decreased with increasing impacting angles. In addition, there is no positive pressure to be discovered at -30° impacting angle for all 4 cases. This phenomenon may be caused from the drag force occurred in the opposite zone of x-direction motion of sphere. For the further understanding, the extra experiments are necessarily required in the future study. Figure 10 also reveals that the rising time periods of the peak pressure increase when the impacting angle larger and smaller than 0°. Within 0.02 second time-series pressure records at 30°, 15° and 0° impacting angles, the pressures are eventually back to zero for the 0°. However, this kind of situation cannot be found for 30° and 15° impacting angles. On the other hand, the sphere continually receives pressure within 0.02 second from the sphere firstly impacting the static water surface. For the impacting angles of -15°, the pressures gradually become negative and stay the constant after several peak pressures aroused. The different time-series pressure pattern of each impacting angle is also observed; even so, the pressure patterns are very similar in the same impacting angle between different cases. The largest pressure among 5 impacting angles happened when the impacting angle equals to zero; at this impacting angle, the pressures suddenly rise to the first peak value and immediately fall in to a negative value. The pressures then rise again to about one-fourth to one-second of the first peak. The summary of peak pressures is shown in Fig. 11.

24
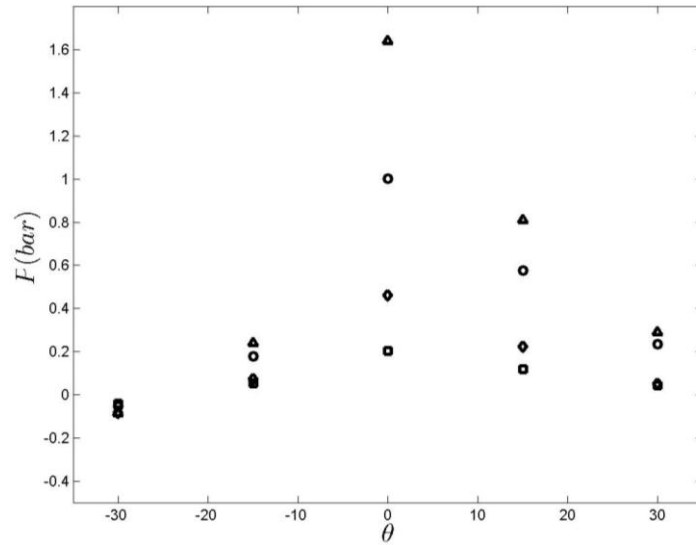
Figure 11. The relationship of peak pressures (bar) and impacting angles (degree). Triangle: Case 4, Circle: Case 3, Star: Case 2, Square: Case 1.

From the figure 11, the peak pressure distributions measured from different impacting angles are greatly distinct. For the impacting angle of -30°, the pressure detected were all negative in all time domains. The range of these negative pressures is between $-0.01 \sim -0.1$ bar and also the narrowest one among 4 cases. For the impacting angle equals to -15°, the sphere receives positive pressures and the range of pressures is about: $0.03 \sim 0.3$ bars, wider than the impacting angle of -30°. For the impacting angle of 0°, the maximum pressure detected is about 1.65 bars and the minimum pressure is around 0.2 bar.

Figure 12. Peak pressures (bar) of each case are as a function of $\sin\theta$: identical zone of deadrise angles.
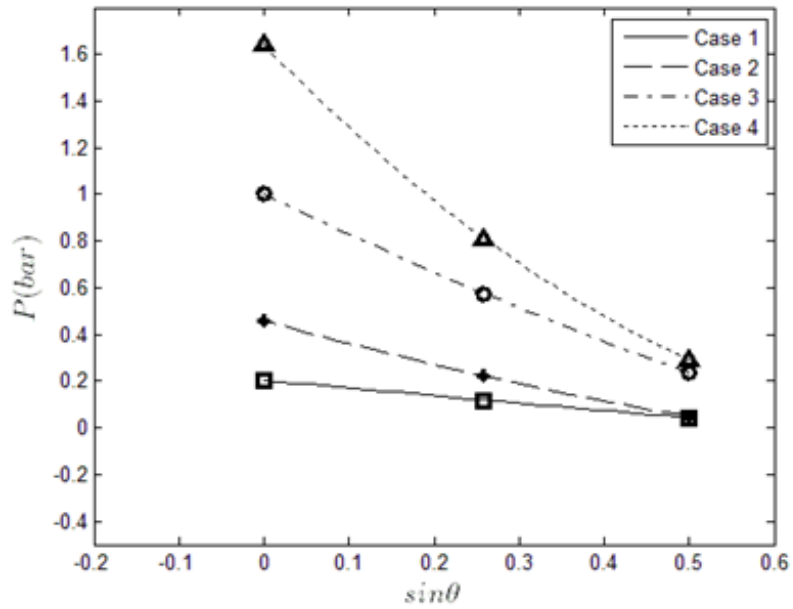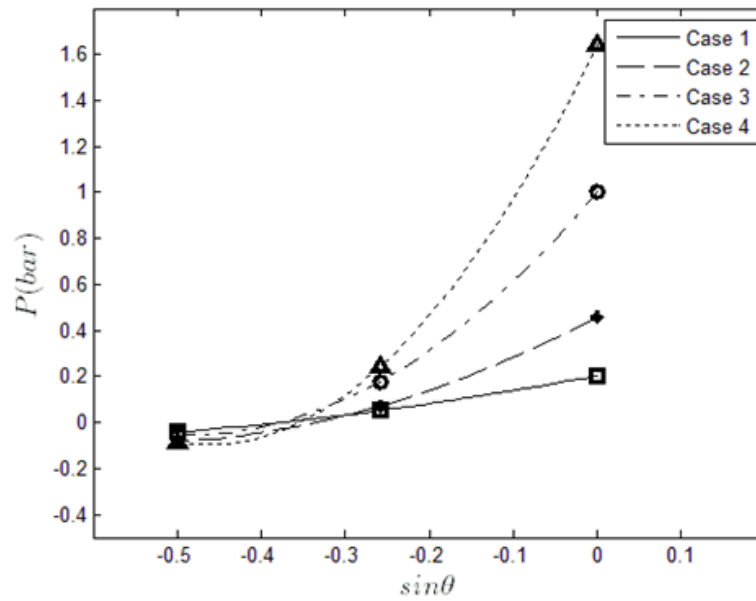

Figure 13. Peak pressures of each case are as a function of $\sin\theta$: opposite zone of deadrise angles.

For the opposite zone (impacting angles of -30°, -15° and 0°), a 2nd order approximation was applied for each different case. The peak pressure is observed as a function of $\sin\theta$, sine function of deadrise angles in the identical zone and the opposite zone, shown in Fig. 12 and Fig. 13. Additionally, the peak pressures at impacting angle 15° are almost half values of the peak pressure at 0° impacting angle. Furthermore, the peak pressure at 30° impacting angle almost is one-third of the peak pressure at 15° impacting angle. The 2nd approximation is appropriate to describe the relationship between peak pressures and relative impacting angles.
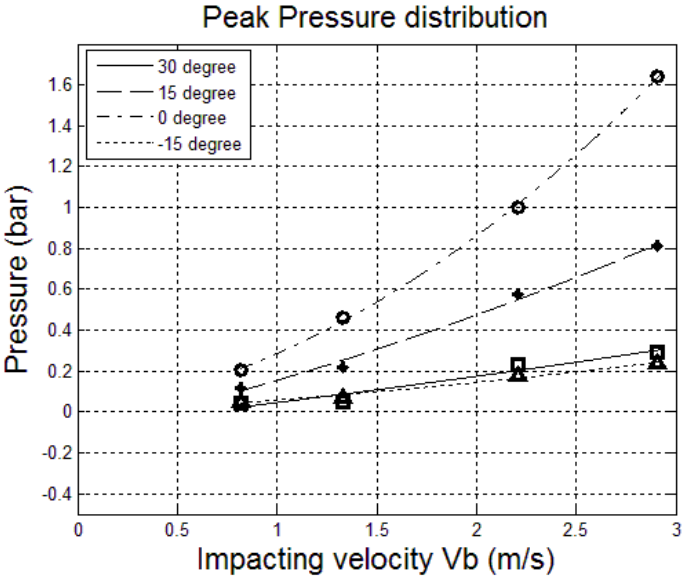
Figure 14. The relationship of impacting velocity V_b and peak pressure. Triangle: -15°. Square: 30°. Star: 15°. Circle: 0°.

Figure 14 shows that measured peak pressures are as a function of impact vertical velocity. The different tendencies are found in different deadrise angles. When the deadrise angles are 30° and -15°, their peak pressures are similar to each other, and the relationship between the impacting velocity and the measured pressure are closely linear though the 2nd approximation The peak pressures is proportiona the impact velocity. Since the pressures have a positive relationship with the square of impacting velocity at the deadrise angles of 0° and 15°, a 2nd order approximation for the impact velocity and the peak pressure was fitted well. The results show that peak pressure at the 0° impacting angle increases rapidly with increasing impacting velocity.

Figure 15. Sphere penetrating quiescent water surface: parameters of calculation.

$$P = \frac{1}{2} C_p \rho U^2 \tag{1}$$

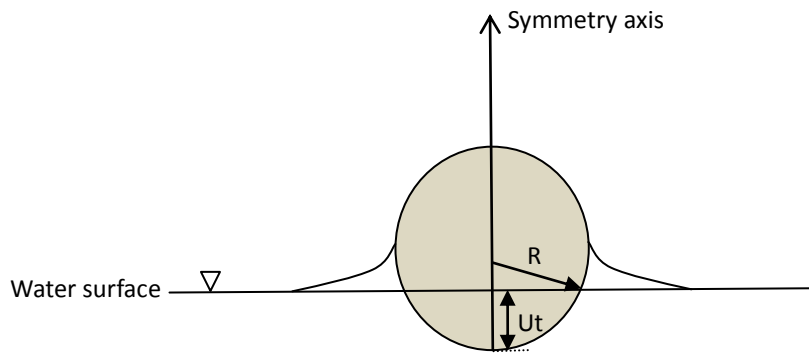$$C_p = 1 - \frac{4(r/Ut)^2}{\pi^2 (3R/Ut - (r/Ut)^2)} + \frac{6}{\pi \sqrt{3Ut/R - (r/R)^2}} \tag{2}$$

An asymptotic solution as equation (2) for analytical pressures presented by De Backer et al. (2009) for hemisphere was compared with sphere slamming experiment results. The asymptotic solution is based on assumptions: potential flow and a constant entry velocity "U". The analytical pressures applied to predict the experimental pressure. However, the use of asymptotic carefully followed the limitations and psychical meanings. The limitation noted by De Backer et al. (2009) between the sphere entry depth and the radius is $Ut/R < 1/5$. The sphere entry depth is defined as Ut, and U is the constant entry velocity, t is time, and R is the radius of sphere. The parameter, r, in equation (2) is the distance between the pressure measurement point and the symmetry axis.

There are three terms included in equation (2) mentioned by De Backer et al. (2009): first term, it is an expression of stagnation pressure; the outcome of permanent flow surround the drop object is the second term; the third term explains the accounting pressure from the expansion. For the pressure measured from the 0° sensor location, "r" is zero.
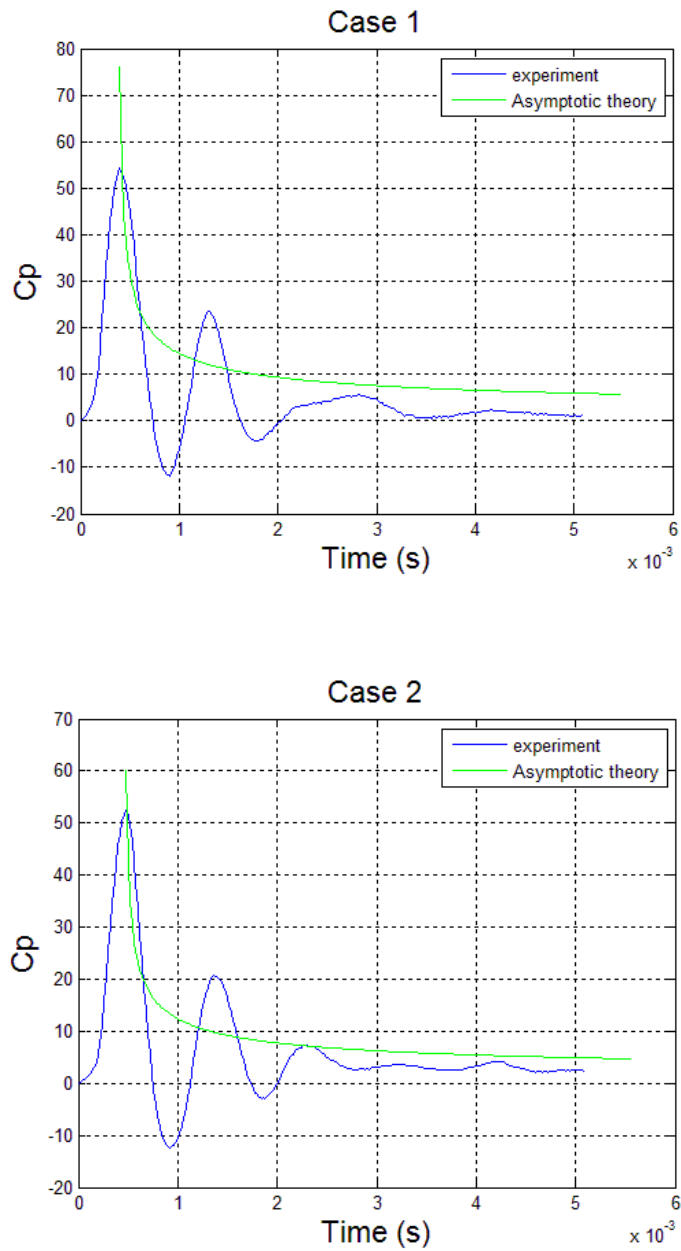
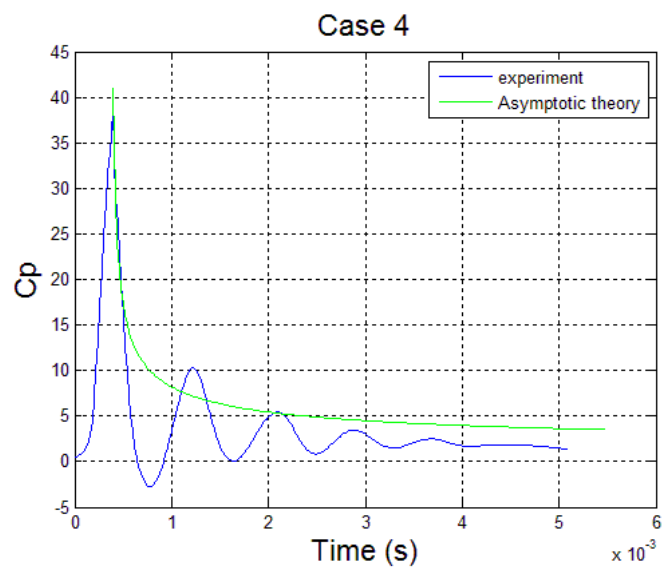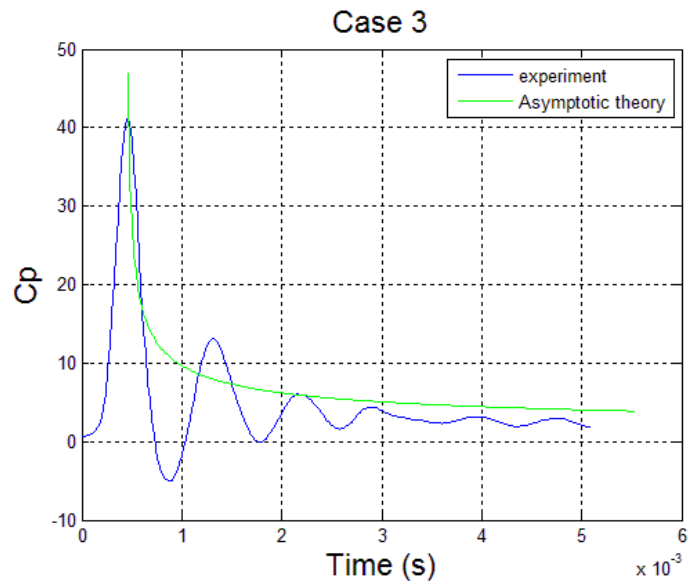**Figure 16.** Measured and theoretical Cp for 4 cases: impact angle 0°.

Figure 16. continued.

The comparisons between time-series slamming pressures measurements and theoretical pressures are shown in Fig. 16. The correlation coefficient between the two set of time series data for case 1 to 4 is about 0.72, 0.65, 0.73 and 0.76, respectively.

The theoretical peak Cp and first peak of experimental Cp is different among the 4 cases. For case 1, the theoretical Cp is about 40% larger than the first peak of measured Cp. Additionally; the theoretical Cp is 14% larger than the first peak of experimental Cp for case 2 and the analytical Cp is around 13% larger than the first peak of experimental Cp for case 3. Furthermore, for case 4 it is just 5% difference between theoretical and first peak of experimental Cp. On the other words, when the impact velocity is larger, the theoretical Cp is more consist with first peak of experimental measured Cp.

Figure 16 also presents that the second peak of experimental Cp is larger than the theoretical Cp. One explanation may be the pressure oscillation of sphere slamming happened in the experiments due to air pocket. The air pocket may exist between the sphere and water surface and cause the oscillation situation. However, the asymptotic theory didn't consider the pressure oscillation resulting from air pocket. Lin and Shieh (1997) and Van Nuffel et al. (2013) demonstrated the zero-crossing pressure oscillation issue mostly happens in the condition of 0° deadrise angle.

The theoretical Cp matches the third peak of measured Cp in the cases of 2, 3, and 4. The third peak of experimental Cp is about 25% underestimated with theoretical Cp in case 1.
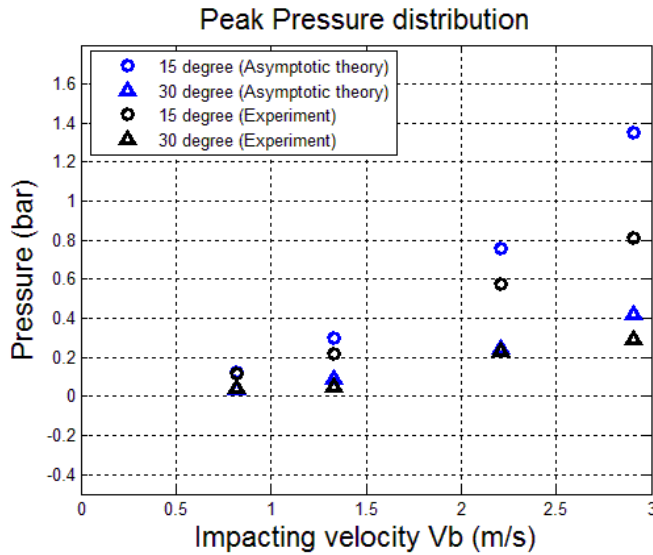
Figure 17. Comparison between theory peak pressures and measured peak pressures.

Figure 17 presents the estimated pressures are overall higher than the experimental values with different degree of magnitudes for both 15° and 30° impact angles. For the case 1 which the vertical impact velocity is around 0.8 m/s, both the theoretical and experimental pressures match each other very well. Obvious difference between theoretical and experimental pressure starts to be found in case 2 with the vertical velocity of 1.3 m/s. Generally, the theoretical values are around 30% higher than the experimental values in case 2.

For case 3 and case 4, when the deadrise angle is equal to 30°, the difference between the theoretical and the experimental peak pressures is not comparatively obvious. The theoretical value is around 25% higher than the measurement in case 4. Meanwhile, the theoretical pressure is almost the same with the experimental value in

case 3.

The big difference can be discovered when the deadrise angle is 15° in case 3 and case 4. The theoretical peak pressure is around 25% over estimated in case 3 and 40% in case 4. These situations also can be found in De Backer et al. (2009). They claimed the ratio between measured and theoretical pressure peak is about ½ and ¾. In this study, the divergence between theoretical and experimental pressure is more significant with higher impact velocity.

The overestimated theoretical peak pressures might be explained as following reasons. A fully rigid sphere is assumed in the Wagner theory; however there might be a slight deformation of sphere occurred at the slamming moment. The energy will be absorbed and the peak pressure will be decreased as Van Nuffel et al. (2013) mentioned. Furthermore, the constant impact velocity assumption need to be studied deeper in order to confirm the theory in the future. Another possible explanation of the divergence between theory and measurement could be the ignorance of the detected area of pressure sensor.
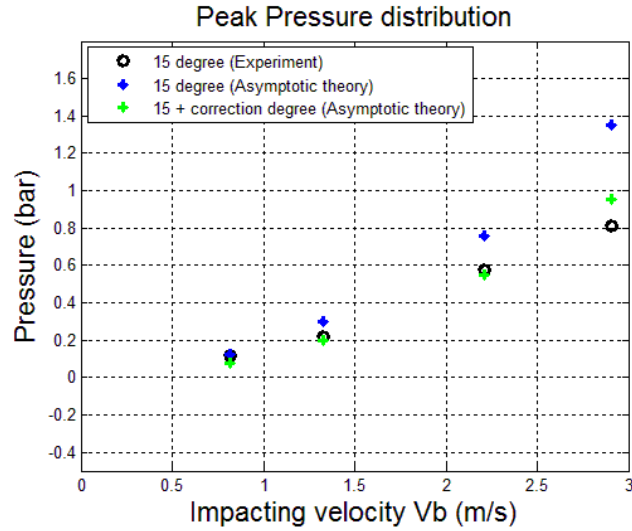
Figure 18. Comparison between the theory peak pressures with impact angle correction and the measured peak pressures: 15° deadrise angle only.

The area of pressure sensor which receives pressures may be a factor to provide the explanation of exist differences between the measured results and the theory. The area affects the definition of the deadrise angle for the calculation of theoretical results. The angle which corresponds with the sensor area was recalculated by Van Nuffel et al. (2013):

$$\Delta\theta = \arcsin(\frac{d_{sens}/2}{R}) \qquad (3)$$

Where d_{sens} is the diameter of pressure sensor. For our pressure sensor, d_{sens} is 1 cm. R is the radius of sphere. We found $\Delta\theta = 3.76^o$ here. Based on the information, the theoretical Cp is recalculated to gain a new set of pressure distribution as the green dots in Fig. 18.

After correcting the theoretical peak pressures, the results between theory and

35

measurement are significantly supported to each other. The difference among case 1, case 2 and case 3 is roughly only 1% at this stage. However, the difference in case 4 is around 17%. Although big difference exists in case 4, it is already narrower than the previous one estimated by asymptotic solution. The theory for the estimation of pressures considering the sensor area is a convenient formula for the slamming issues, even the existence of overestimated different degree.

We reconsider that the theoretical pressure peaks are distributed uniformly over the entire sensor area versus various deadrise angles. An averaged pressure profile over sensor area is introduced by Van Nuffel et al. (2013):

$$C_{p,average} = \frac{\int_{\theta-\Delta\theta}^{\theta+\Delta\theta} C_p d\theta}{2\Delta\theta} \tag{4}$$

Experimental pressures, asymptotic pressures, and averaged asymptotic pressures are compared in Fig. 19. The peaks estimated from the asymptotic theory are the highest, and the approximations of averaged asymptotic theory are much lower than the measured peaks. The pressure peaks from the averaged theory are generally half of the measured peaks. However, the relationship between the measurement and average theory is not obvious in our study. Nevertheless, the asymptotic theory is still quite practicable for our study especially after considering the extra sensor area of deadrise angle.

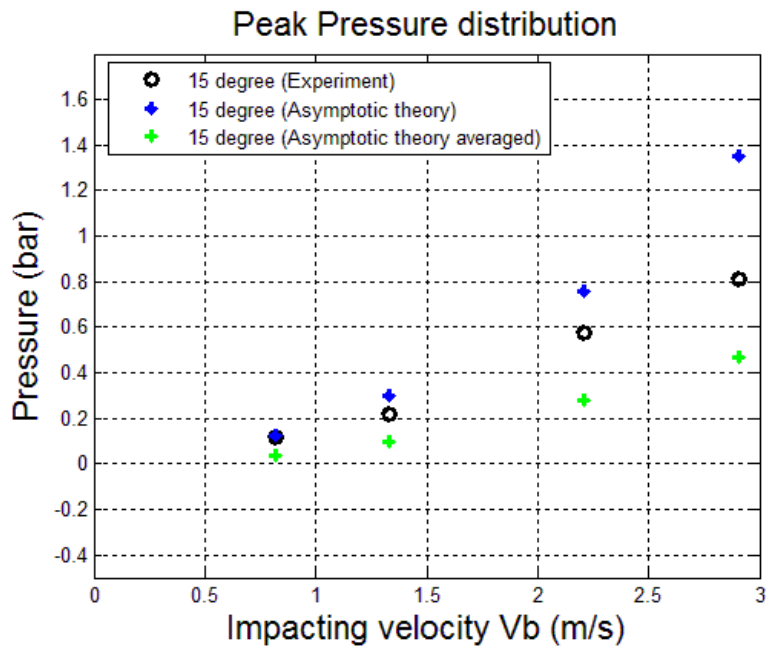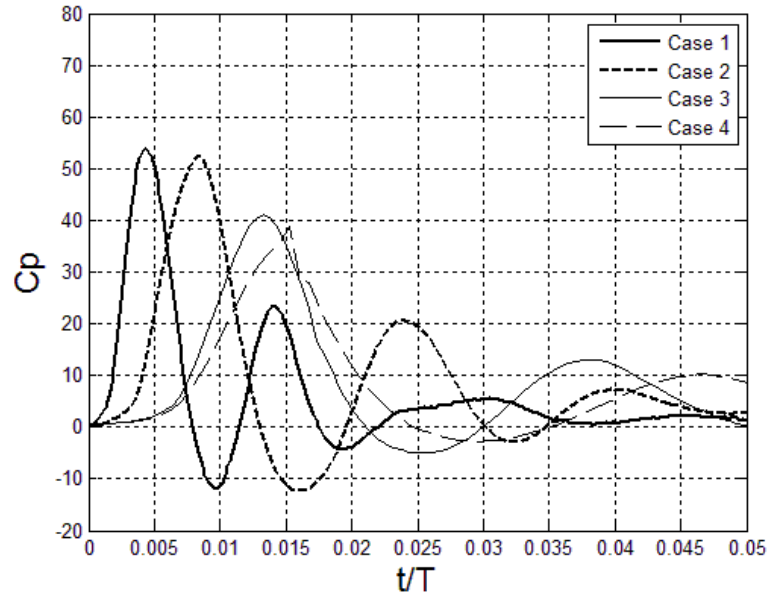**Figure 19.** The comparison between the theory peak pressures with averaged impacting angle and the measured peak pressures: 15° deadrise angle only.
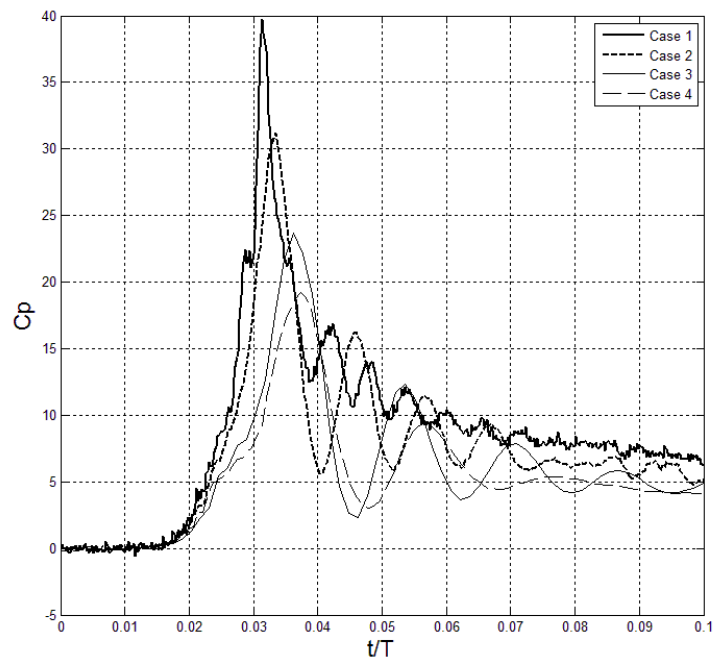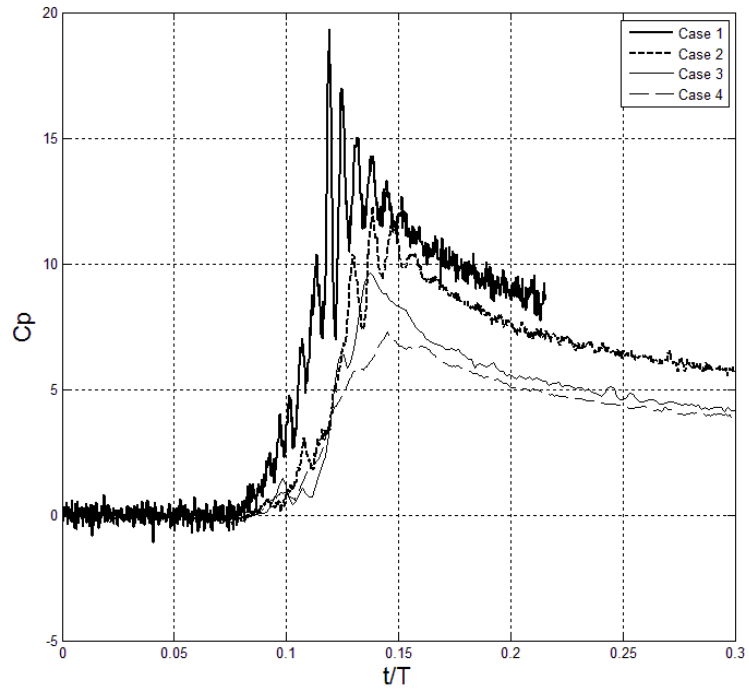
0⁰

15⁰

Figure 20. Time series measured pressures: 4 cases with 4 impacting angles

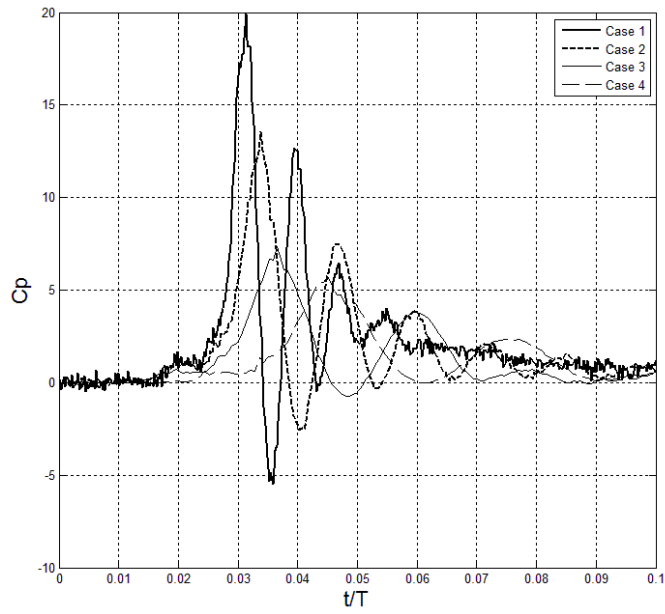**30°**

-15°

Figure 20. continued.

Figure 20 presents the time series of C_p, in which time is normalized by "T". Where T is D_{sphere}/V_b and depends on the each impacting vertical velocity V_b for each case, T is different here.

For the 0° degree impacting angle, the pattern of the four cases could be distributed into two groups based on the values of peak C_p : case1 and case 2; case 3 and case 4. For case 1 and case 2, the peak C_p is about 50, and the peak C_p is around 40 for case 3 and case 4. Also, the moments of the peak values occurred are not consistent. The moments for case 1 to case 4 are happened in 0.004, 0.008, 0.012 and 0.015, respectively, summarized in table 3.

For the impacting angle of 15°, the C_p values are decreased with increasing the impact velocities. C_p for case 1 to case 4 are about 40, 32, 28 and 18, respectively. There is no zero-crossing oscillation occurred at the non-zero impact angle.

For the 30° impact angle, the patterns among the four cases are very similar. However, the peak C_p values are also decreased with increasing impact velocities.

For the -15° impact angle, the same situation of peak pressure distribution can be observed as the impact angles of 15° and 30°. The peak C_p values are similar to the case with the impacting angle of 30°. The reason for the difference between 15° and -15° impact angles may be the existence of the horizontal impacting velocity of x-direction toward to the positive impacting angles. Thus, the further study is necessary in order to fully accomplish the relationship between the velocity which is parallel to the static water surface and the slamming pressure. Although the peak pressures vary with the impact velocities, the pattern of the time-series pressures is very similar in the same

deadrise angle.

Table 3. The summary of peak pressures versus C_p and t/T

Case # versus Impact angle	P_{max} (bar)	$C_p = \dfrac{2P_{max}}{\rho U_z^2}$	t/T
Case 1, 0°	0.204	54.18	0.0043
Case 2, 0°	0.461	52.44	0.0083
Case 3, 0°	1.003	41.22	0.0133
Case 4, 0°	1.641	38.83	0.0153
Case 1, 15°	0.135	39.74	0.0313
Case 2, 15°	0.274	31.19	0.0334
Case 3, 15°	0.576	23.66	0.0362
Case 4, 15°	0.811	19.20	0.0374
Case 1, 30°	0.065	19.31	0.1193
Case 2, 30°	0.108	12.26	0.1384
Case 3, 30°	0.234	9.64	0.1375
Case 4, 30°	0.307	7.26	0.1450
Case 1, -15°	0.068	19.92	0.0313
Case 2, -15°	0.119	13.54	0.0337
Case 3, -15°	0.178	7.32	0.0365
Case 4, -15°	0.243	5.76	0.0450

CHAPTER IV

JETTING FLOW INVESTIGATION

The slamming pressures were investigated as pervious section. This chapter will focus on the examination of jetting flow field. The two-dimensional jetting flow fields of 4 different impacting velocities are introduced.

The jetting flow caused from the sphere slamming could be revealed by a series of images taken by high speed camera. This jetting phenomenon happened almost immediately after the occurrence of contacting between the sphere and water surface, so the frame rate of the camera needs to be high enough in order to catch the jetting situation. The frame rate of the camera is 12 kHz.

Time-series jetting speeds were able to be gained with different frame rate comparing with Thoroddsen et al. (2004) by BIV approach. The two-dimensional time-series of whole field jetting speed distributions were also investigated.
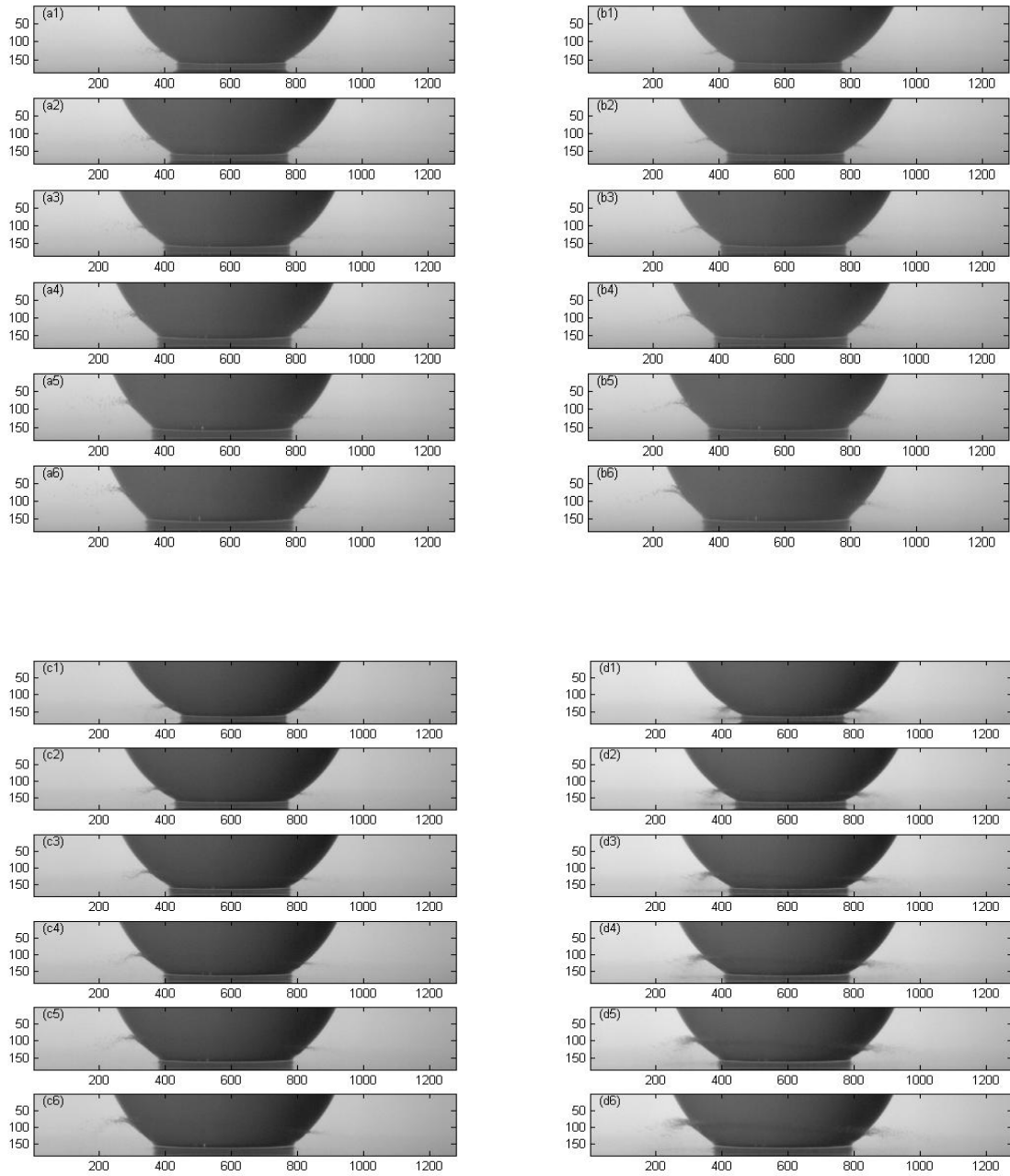
Figure 21. Time-series raw images of 4 cases. a: case 1, b: case 2, c: case 3., d: case 4. One pixel equals to 0.2 (mm).

44

Raw images from the high speed camera of jetting flow are displayed in Fig. 21, and the evolution of the jetting filed could be observed of 4 cases. The "time" was defined as normalized t/T and $T = D/V_b$ with respected to the vertical velocity of sphere of each case. The non-dimensional time series from the top to the bottom in each case of raw images is 0.032, 0.038, 0.044, 0.050, 0.057 and 0.063, respectively. Jetting flow particles are clear in the raw images as the relative darker spots. The BIV technique is applied to evaluate velocity fields after converting the raw images to the inverted images.

The pattern of the jetting flow is similar in each case at the same normalized time stage. Jetting flow arouses as a sheet with finger-like shape. The same shape was figured out as Thoroddsen et al. (2004). The front of jetting flow gets higher and further over time.

Although the overall situations of jetting flow in 4 cases have the same tendency, the differences between four cases are still found. The jetting sheet is very thin in case 1 and the flow particles are easily observed as gray dots in the raw images especially in the front of jetting. At the same time, the jetting sheets are thicker when the impact velocities are higher. Meanwhile, the jetting particles are finer and no longer easily distinguished in the raw image of case 4. The closer view of these jetting particles is shown later.

A.

Figure 22. Jetting flow fields of case 1. (A) Velocity vectors. (B) Velocity contours.

B.

Figure 22. continued.
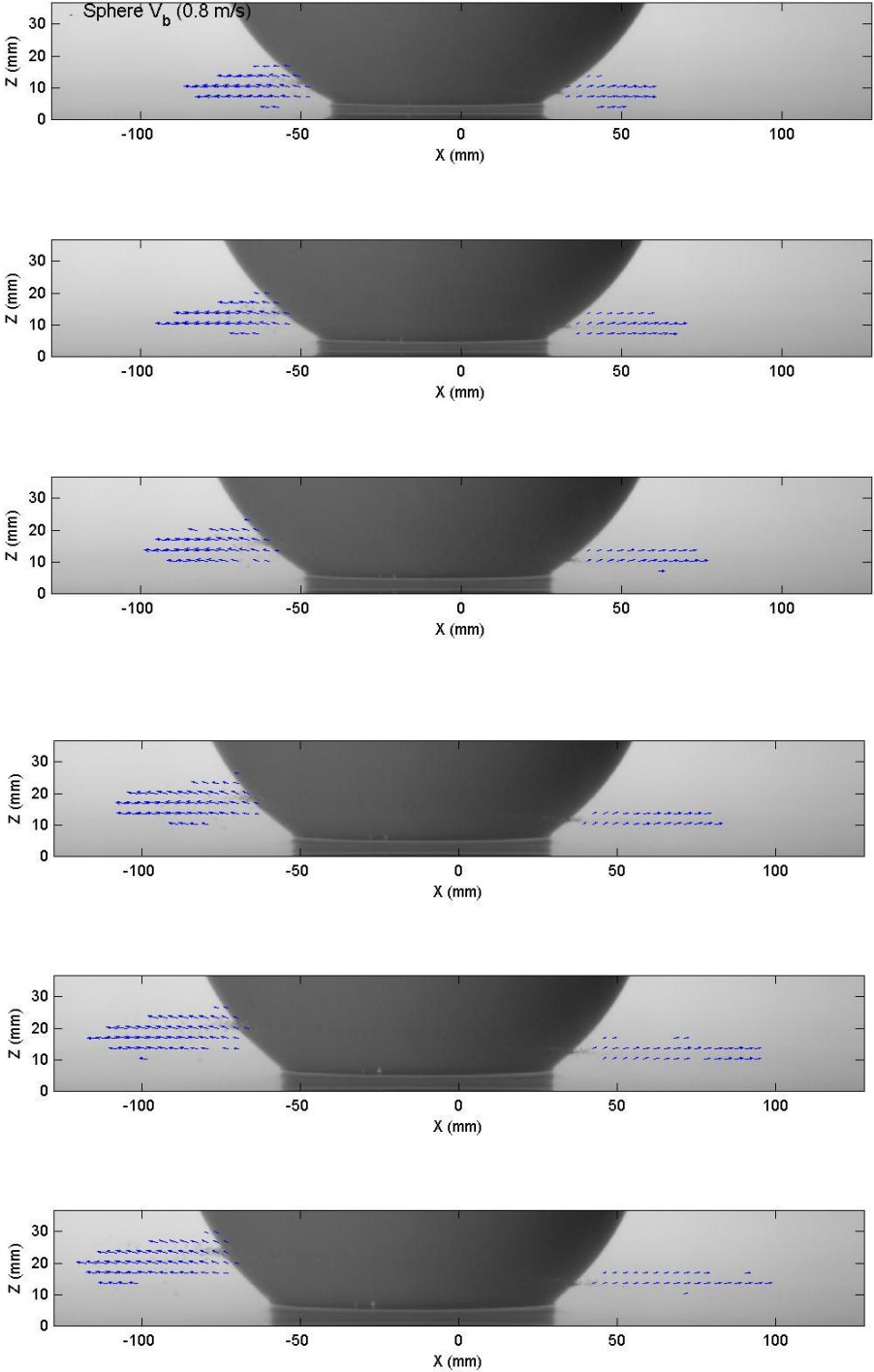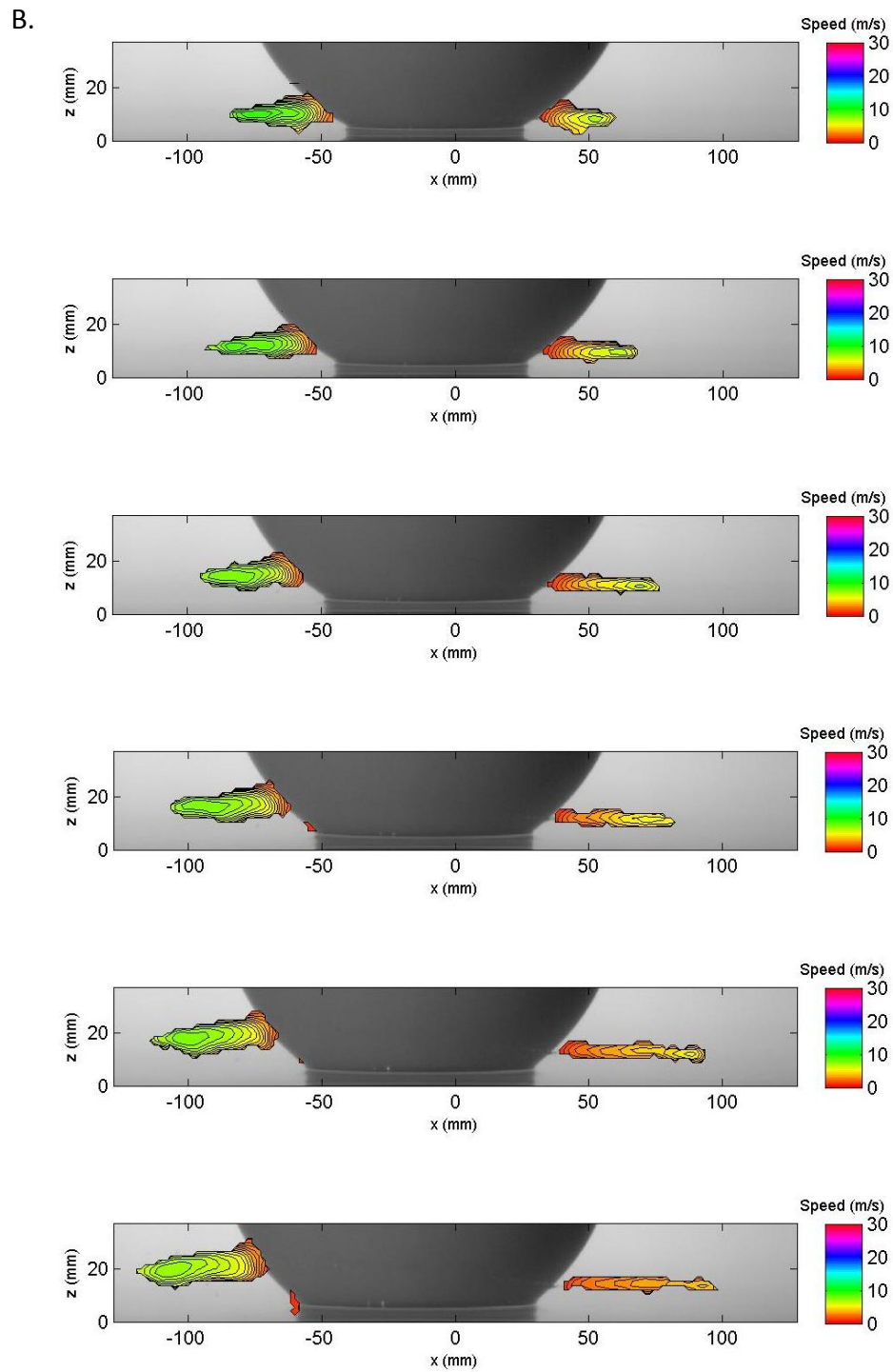
A.

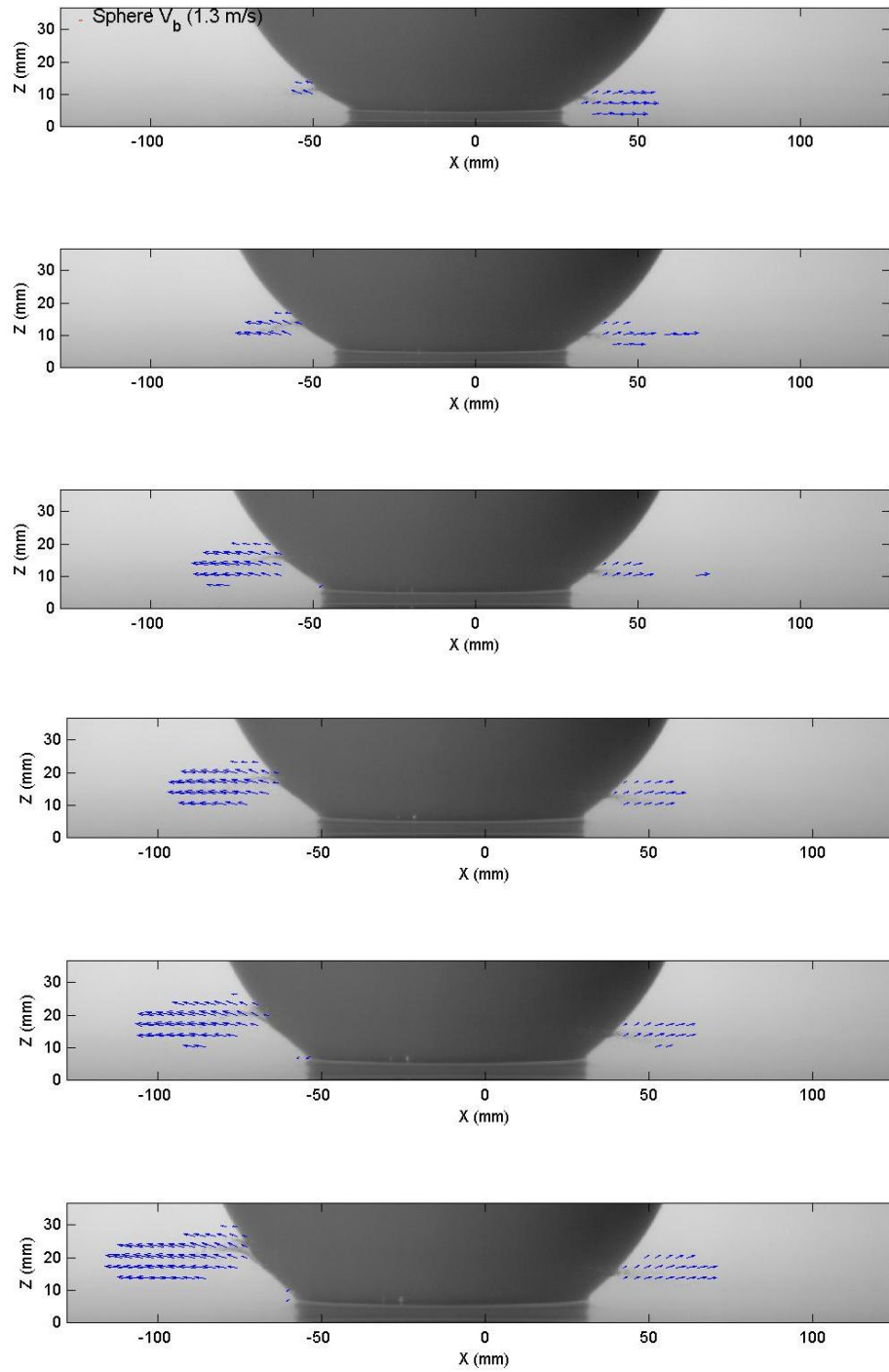**Figure 23.** Jetting flow fields of case 2. (A) Velocity vectors. (B) Velocity contours.
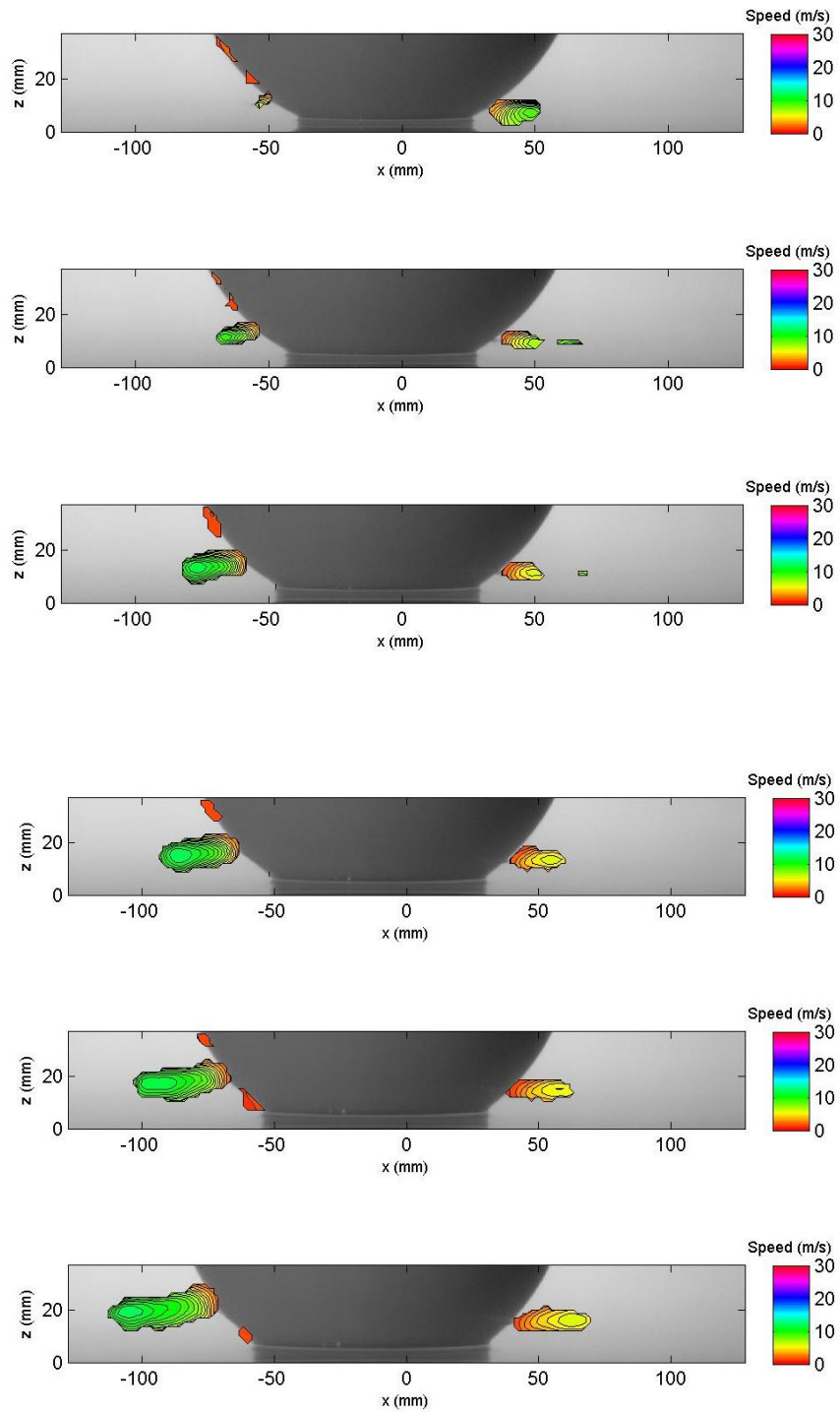
B.

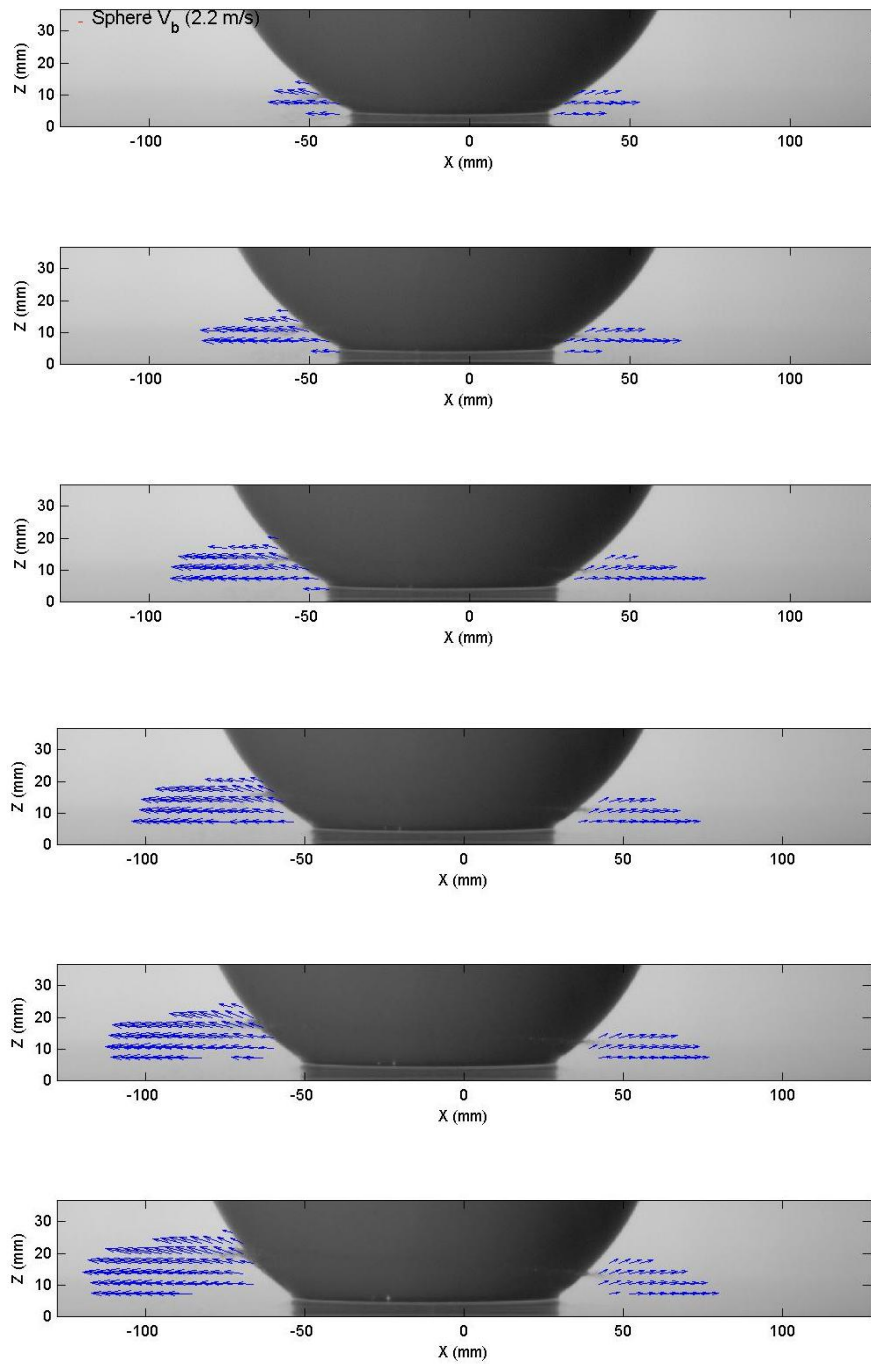**Figure 23.** continued.

A.

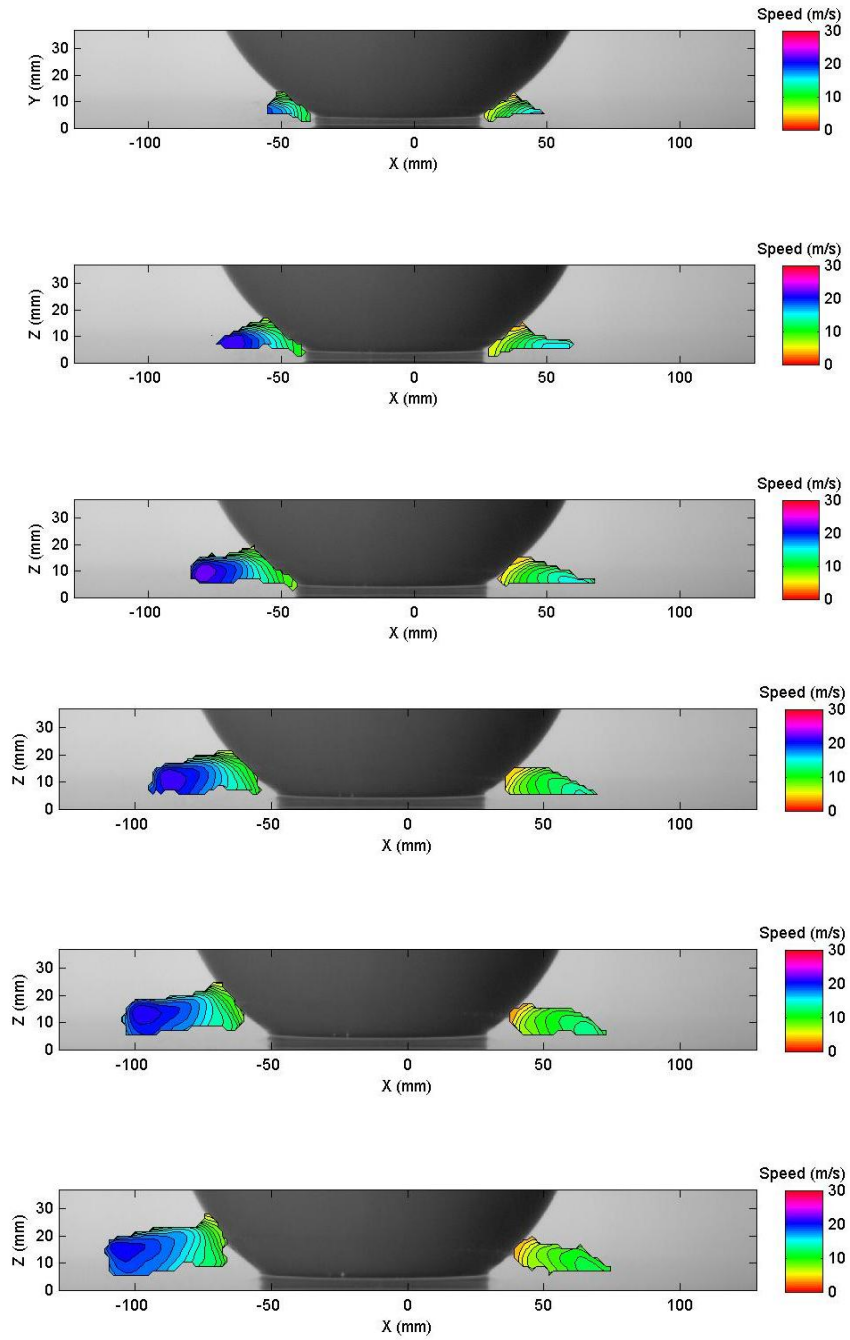**Figure 24.** Jetting flow fields of case 3. (A) Velocity vectors. (B) Velocity contours.

B.
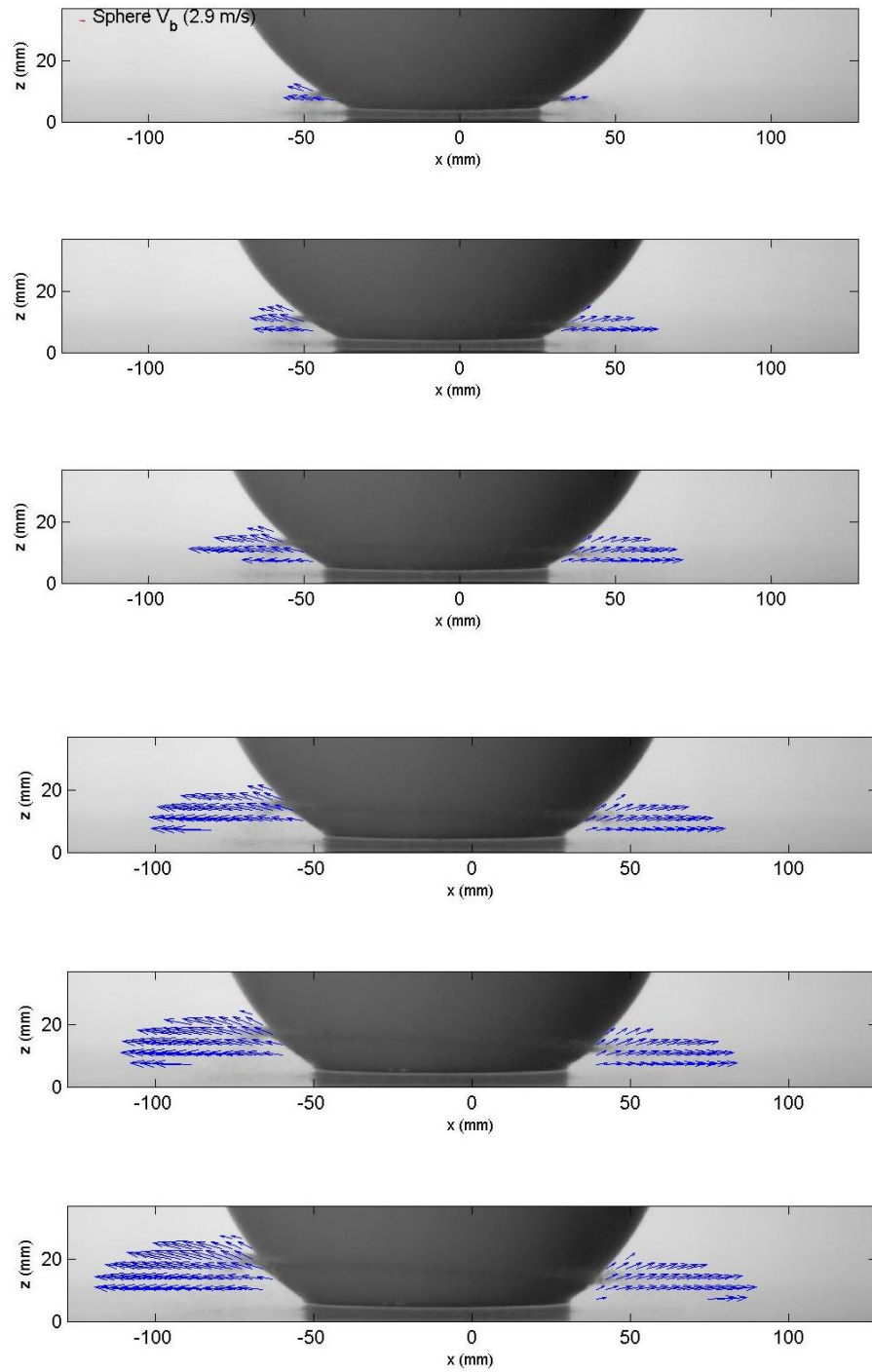

Figure 24. continued.

51

A.

Figure 25. Jetting flow fields of case 4. (A) Velocity vectors. (B) Velocity contours.
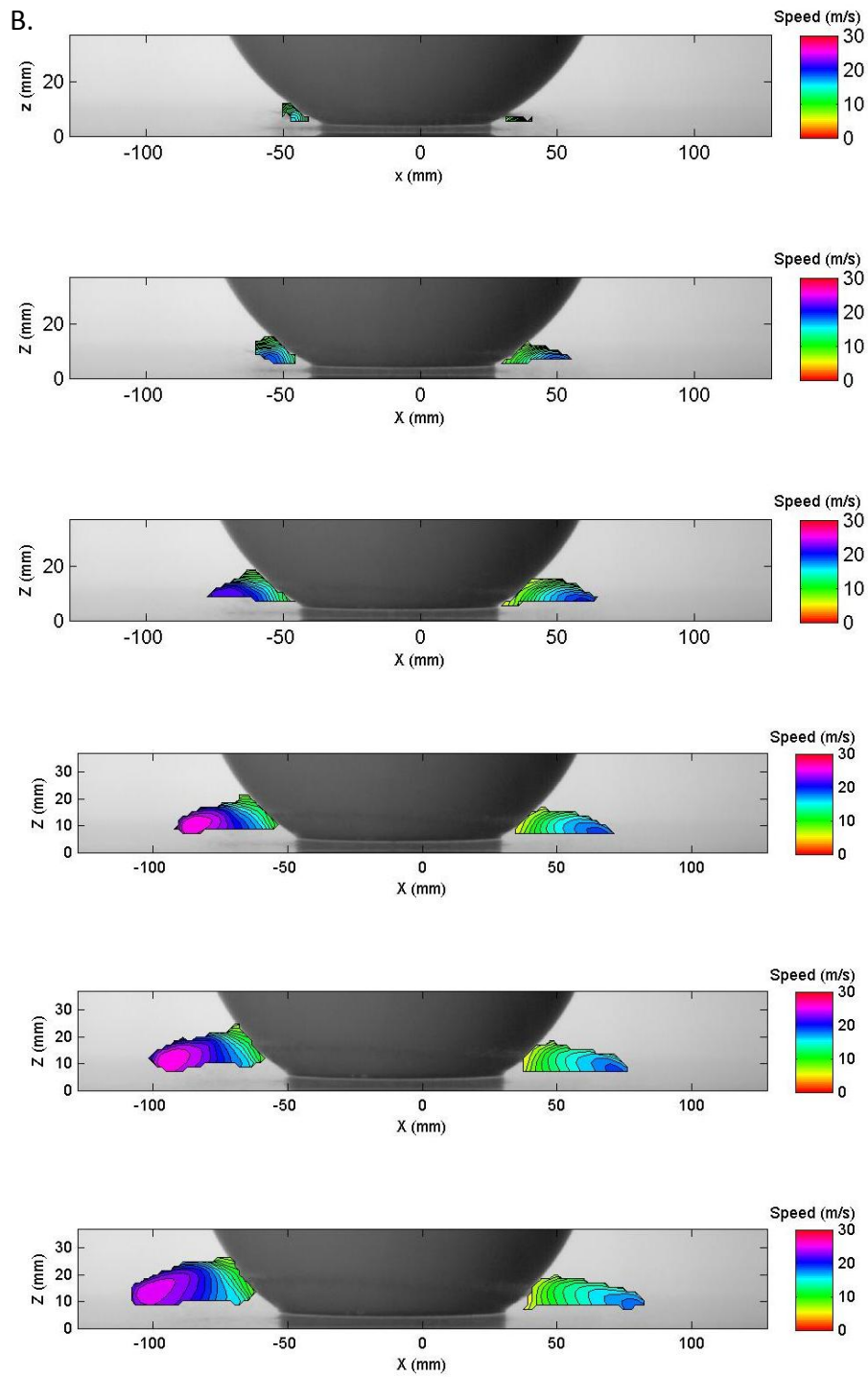
Figure 25. continued.

From the figure 22~figure 25, normalized time-series jetting flow velocity fields and contours are presented for 4 cases. Section A of each figure is the velocity vectors and section B is the velocity contours. The velocity vectors shown above are the mean values from 20 repeated measurements. The contours were obtained by averaging 20 measurements. In the meantime, the background pictures were random selected from 20 sets of measurements. The whole experimental fields of jetting flow speed evolution for 4 cases are illustrated. The sphere has not only the vertical velocity but also horizontal velocity toward to left direction of the figures. Each jetting flow velocity field is not symmetric with the symmetric axis of sphere.

Figure 22 shows the development of jetting for case 1. At the first time stage, that is 0.032 of non-dimensional time frame and it is around 0.0059 s of the real time. The jetting flow speed is about 10 m/s and it is 12 times higher than the vertical impact sphere speed. the jetting flow speed of 10 m/s is not the highest jetting flow speed in case 1. The maximum jetting flow speed is about 12 m/s and happened in 0.0027 s after the sphere firstly impacted water surface.

The jetting flows continue to go further higher even the maximum speed decreased gradually through the rest of time frames. The deceleration is around 540 m/s^2 in this case, which is very large because the jetting flow happened in the very short time period. The jetting flow deceleration conditions are also presented by Yoon et al. (2007).   From the contours of case 1 the max speed happened in the front of jetting flow in six time frames. This phenomenon could be observed also in the other cases. At the first time frame, it is in the very initial stage of the jetting flow development. The

54

jetting flow was already well developed in case 1. However, at the same

non-dimensional time frame, the jetting flows were not easily observed in other three

cases, especially in case 2. The reason might be the turbulence in case 2   that happened

at the initial stage is higher than the other cases and the jetting flow speed is not easy to

capture, shown in Fig. 28.

The velocity vectors and velocity contours of case 2 are displayed in Fig. 23. The

maximum jetting speed is about 13 m/s and it happened at 0.0051 s of real time. The

max speed in the contour is presented as the purple circle at the third time frame. The

max speed of case 2 is around 11 times of its sphere vertical speed.

The direction of the jetting flow speed can be learned as the velocity vectors. The

horizontal component of the jetting speed is dominant especially near the front of jetting.

The significant x-direction velocity drives the flow moving apart from the sphere. The

occurrence also can be found in the other three cases. The real time-series maximum

speed of vertical and horizontal components will be shown in the later section of all four

cases.

The maximum jetting velocity happened of case 3 is about 0.003 s of real time

scale. It was examined between the second and third non-dimensional time frames. The

max jetting velocity is about 23 m/s and it is 10 times of vertical sphere speed in case 3.

Furthermore, the max jetting velocity occurred at 0.0025 s in case 4. It is shown on the

contour of the third time frame in Fig. 25. The max velocity in case 4 is about 9 times

larger than the sphere velocity of vertical direction and its value is 27 m/s, observed in

Fig. 27.

When the vertical sphere velocity is higher, the shorter time of the max jetting flow velocity occurred is required. The max jetting flow velocity is about 9~13 times of their vertical impacting sphere velocity. On the other hand, the jetting flow velocity is much higher than the impacting velocity. The jetting flow velocity of x-direction is the leading component and the maximum jetting velocity travels as the front of the jetting sheet. During the short time period, the jetting continues moving upward and further away from the sphere even the maximum velocity decreased in all four cases. Furthermore, the jetting goes with different magnitudes of horizontal velocity in identical zone and opposite zone.

Figure 26 presents the path line in the identical zone and the opposite zone. The patterns of path lines of the identical zone are similar in four cases. The reason is the similarity for the ratio of the vertical jetting velocities and horizontal velocities among all four cases, resulting in consistent path lines. However, , the requirement of total duration for completing the path lines for each case is not the same due to the divergence of the horizontal jetting velocities. The path line is the path of the maximum jetting velocity at each real time frame; it is not a real tracking line for a single water particle from the beginning to the end. Thus, the path line just offers an idea about the movement of jetting. The path lines of the opposite zone are not as uniform as in the identical zone. The reason might be the drag force occurred at this zone, and another possible reason may be the uncertainty of velocity field. However, the jetting measurements have relatively accurate because of consistency of the jetting flow path patterns in the identical zone and the turbulence intensity contour of the jetting flow field.
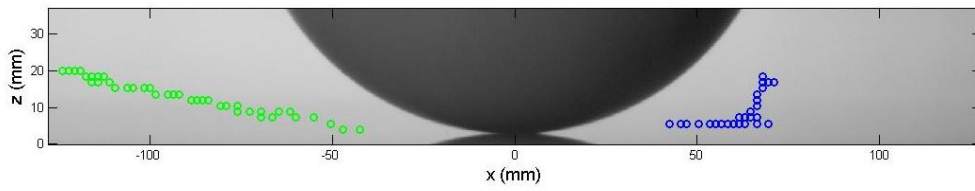
56

Case 1:
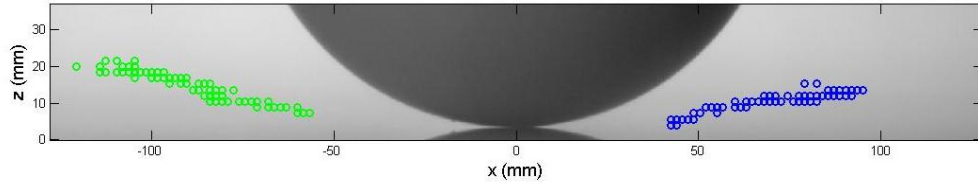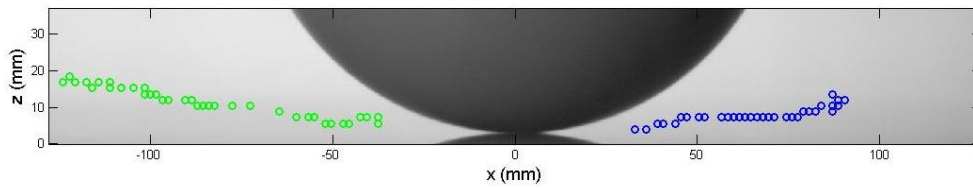

Case 2:
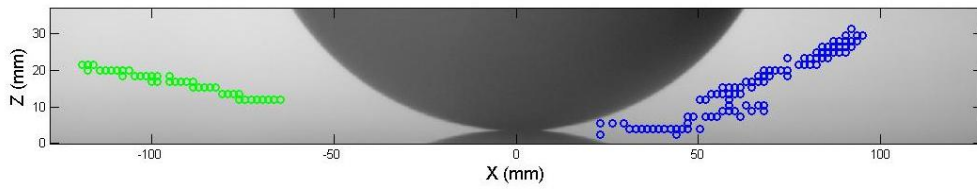
Case 3:

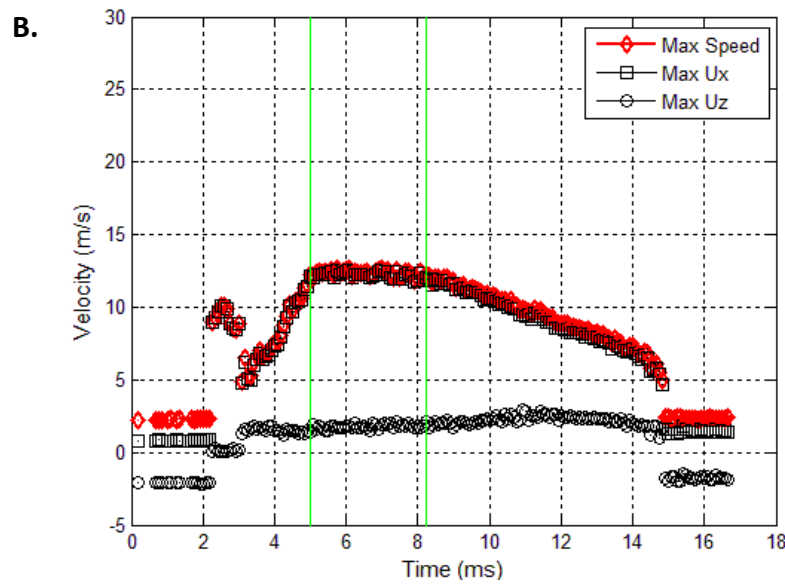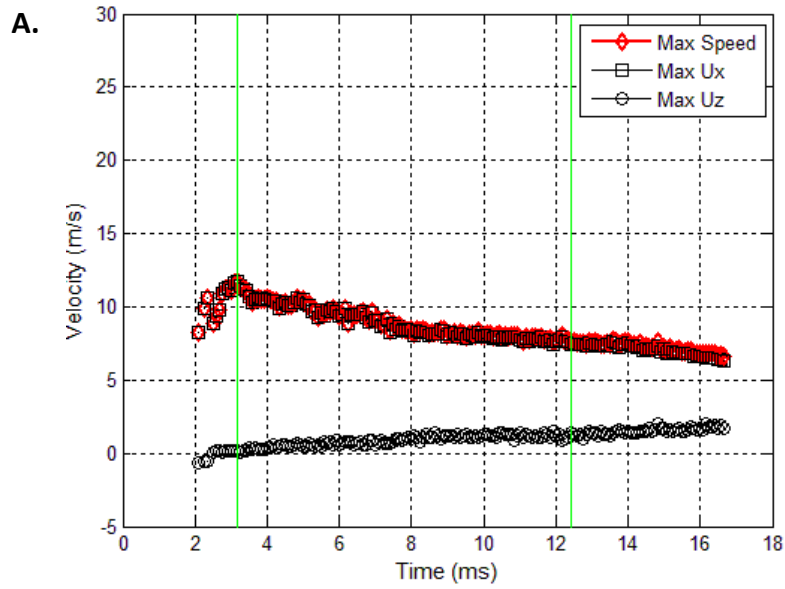Case 4:

Figure 26. Path line of max jetting speed.

Figure 27. Time-series max velocity of 4 cases in the identical zone. Green lines indicate the moment of max velocity occurred and the moment of the flow field starts to be out of the experiment images. (A) Case 1. (B) Case 2. (C) Case 3. (D) Case 4.
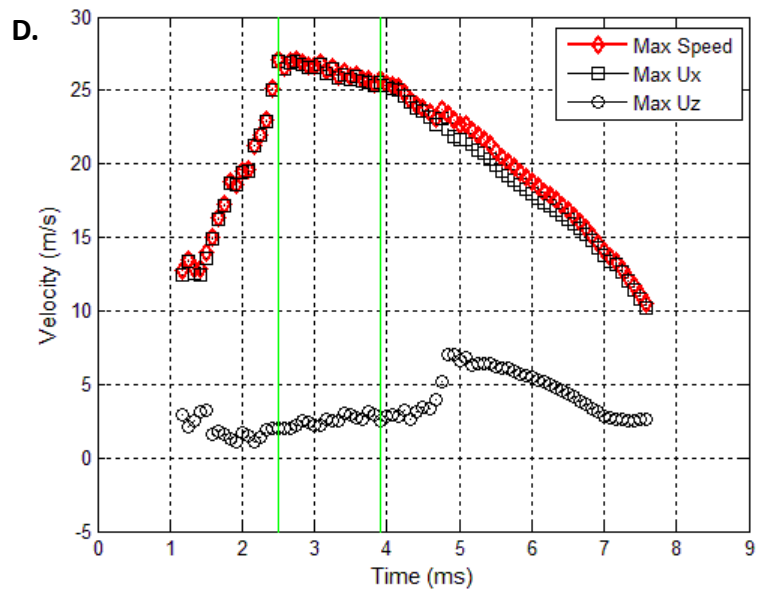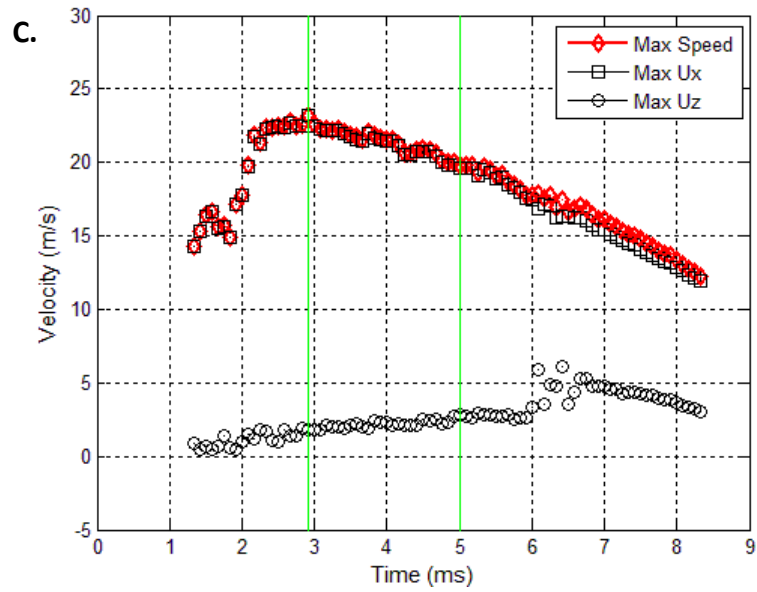
Figure 27. continued.

Figure 27 shows the time-series maximum velocity and corresponding maximum Ux, the horizontal component of velocity, and Uz, vertical component velocity. Acceleration can be found in the four cases at the initial stage of speed records with different acceleration rate. This acceleration occurrence also revealed by Jepsen et al. (2006). They found that there are three stages of ejected water particles caused by impact: rest, acceleration and deceleration. The ejected water particles stay as rest when the impacting initially happened. The particles experienced the acceleration through the compacted air and then the speed decreased by the drag from air.

Our study also has these three stages shown in Fig. 28. The conclusion here may be against the statement that the maximum value of jetting flow speed showed when the jetting occurred initially, mentioned by Thoroddsen et al. (2004).

There are some differences of experimental set-up and concept between Thoroddsen et al. (2004) and our work. First, the frame rate of their camera is very high as 100 kHz~1 MHz. Secondly, the range of their impact Reynolds number is larger than our study. Finally, different kinds of fluid with several viscosities are used for their experiments. Due to the above reasons, the three stages we detected might be differed from their work.
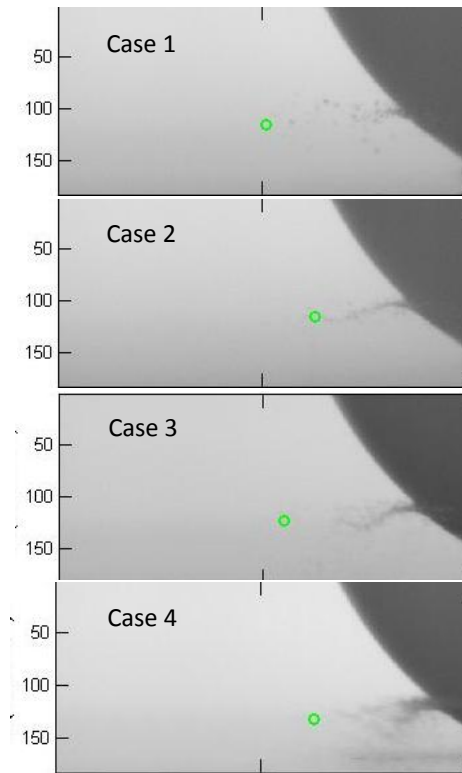
Figure 28. t/T = 0.044 of 4 cases. The green spot is the location of corresponding max jetting speed occurred. The scale is pixel and 1 pixel = 0.2 (mm).

Figure 28 shows the location of the max velocity happened at the normalized time frame of 0.044. According to our study, maximum velocity is emerged in initial beginning stage of jetting flow. The jetting particles with the max velocity moved forward and upward as the front of entire flow field over time. Because of the friction from air, the max velocity decreased over time but is still emerged at the front of the flow field. The background in Fig. 28 is randomly selected from 20 repeated measurements.

Case 1:
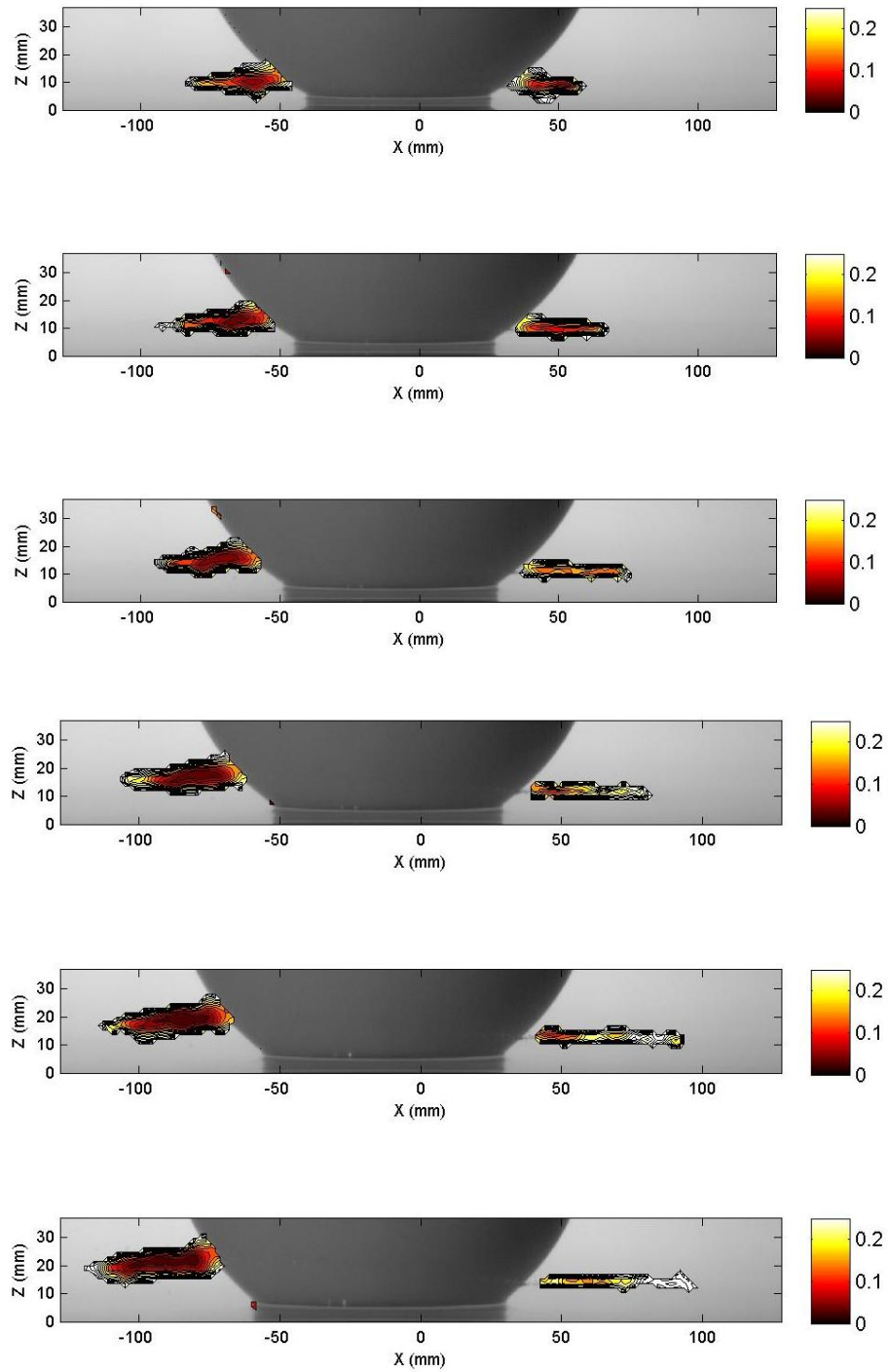
Figure 29. Normalized turbulence intensity.

Case 2:

Figure 29. continued.

63
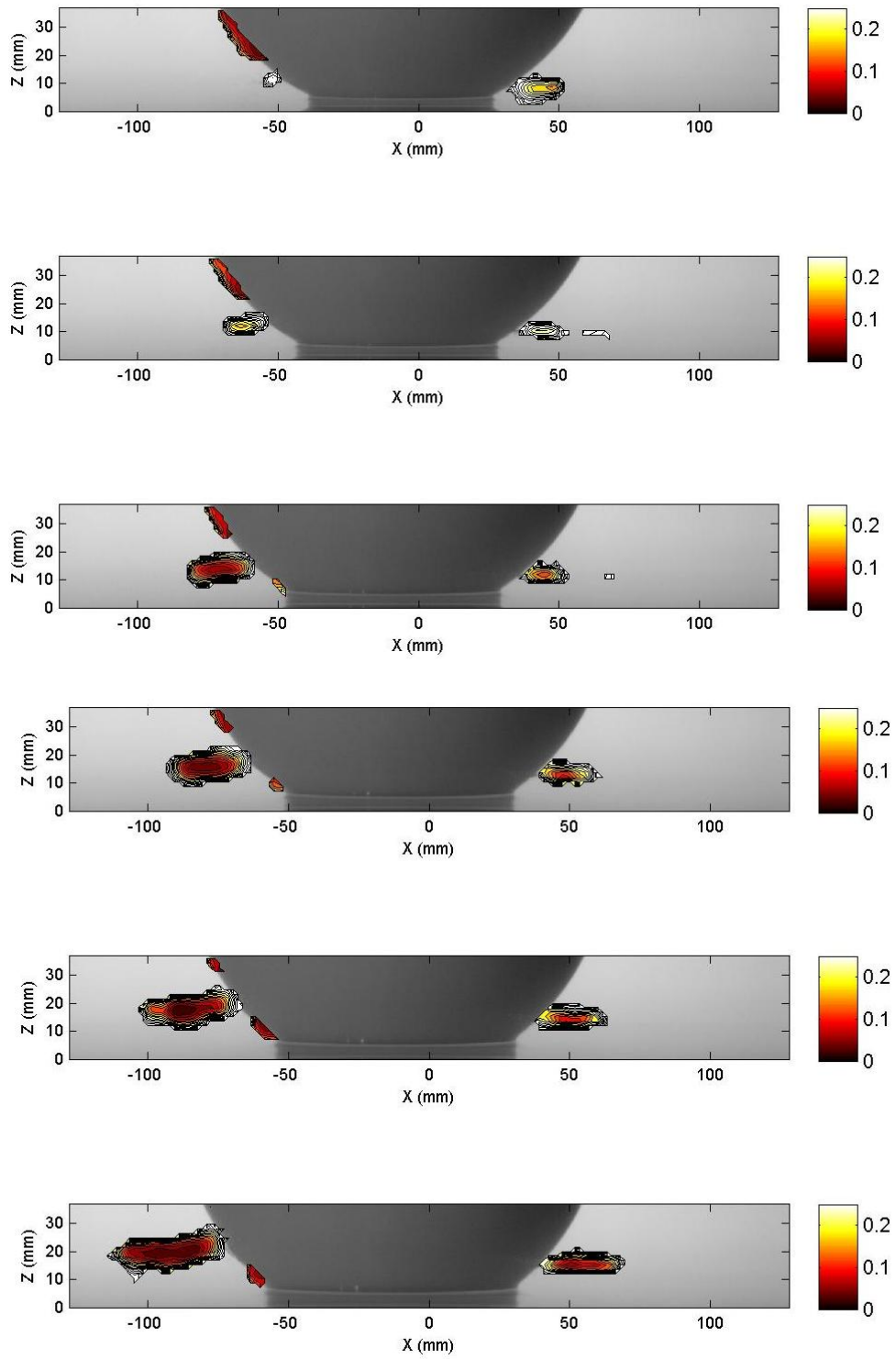
Case 3:

Figure 29. continued.

64
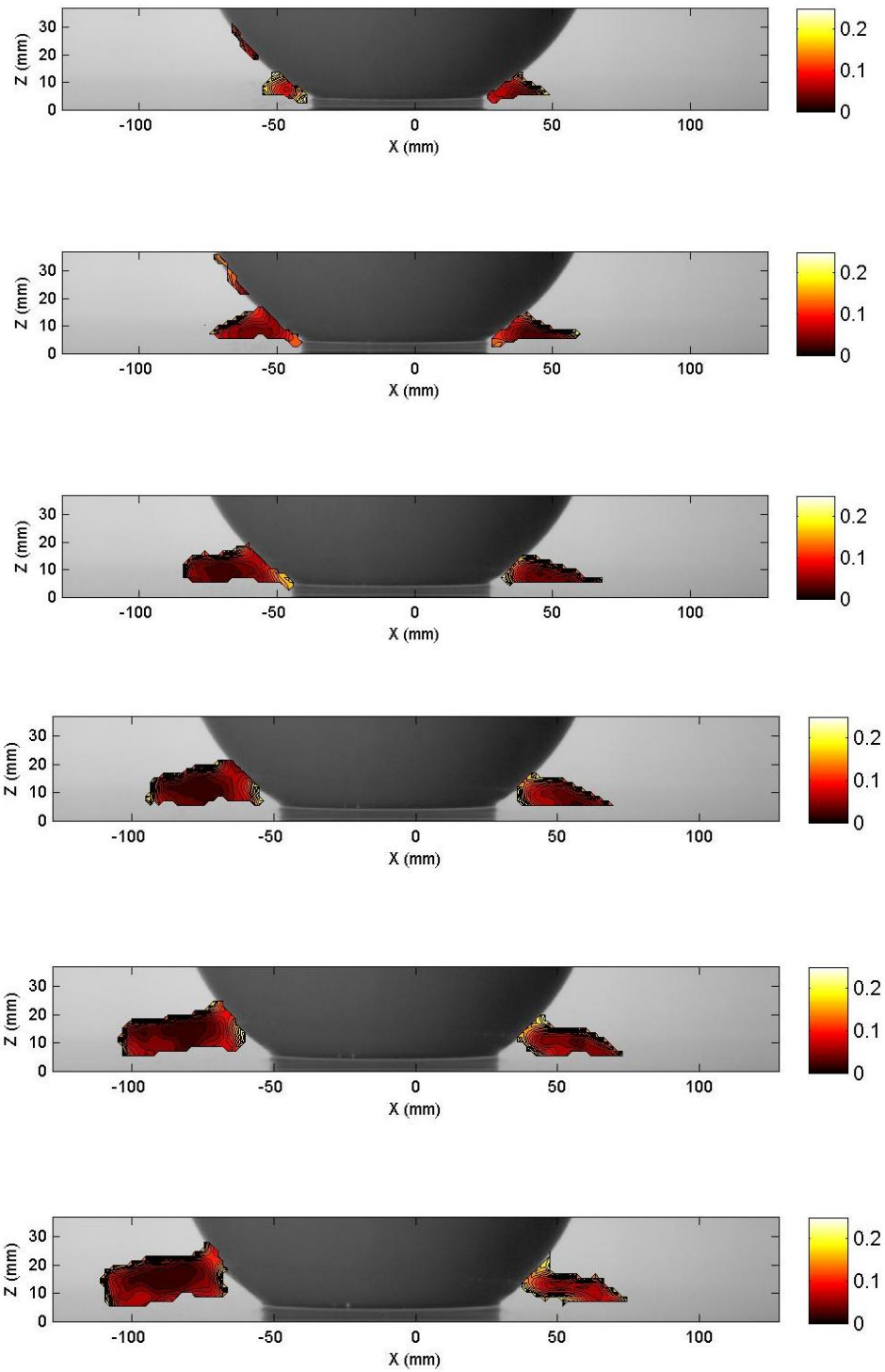
Case 4

Figure 29. continued.

65
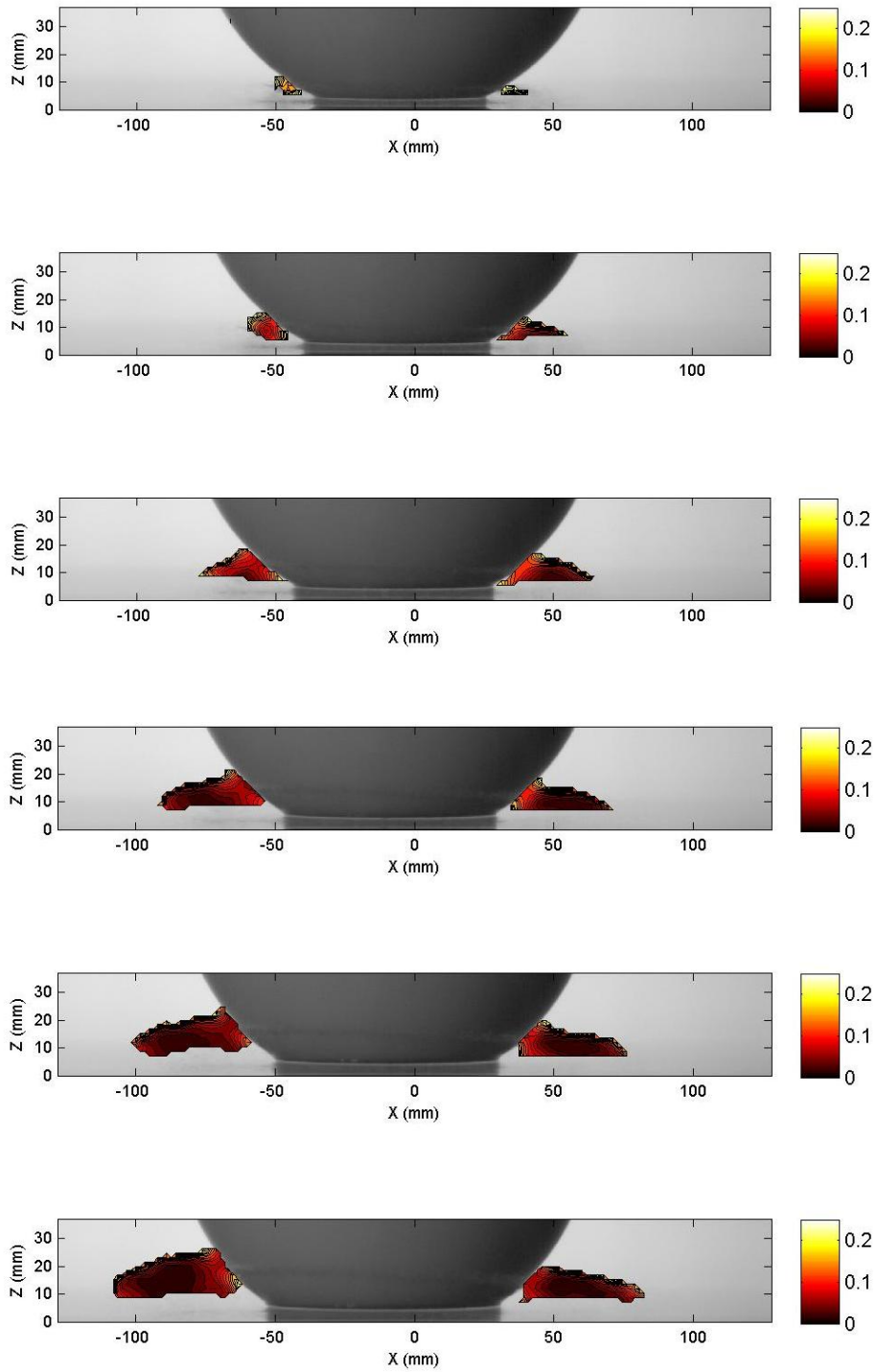
A series of turbulence intensity contours with non-dimensional time frames corresponding to the velocity vectors and velocity contours are shown in Fig. 29. The turbulence intensity is two dimensional and calculated as equation: $I = \sqrt{U_x' U_x' + U_z' U_z'}$. Where U_x and U_z are the horizontal and vertical velocity components. The turbulence intensity contours in Fig. 29 are normalized by the sphere vertical impacting velocities in each case.

The distribution of turbulence intensity in each case is similar. The relative lower turbulence intensity mostly concentrated in the middle of the jetting sheets all the time. The turbulence intensity is slightly higher on the other area of the jetting sheets. Especially, the turbulence intensity for some jetting area of case 1 and case 2 reached to 0.25. The turbulence intensities of case 3 and case 4 are generally very low and below 0.1 for most jetting sheet areas. Although the jetting particles are not easy to be distinguished as a one single point at the most time, the jetting particle size of each case needs to be examined carefully to get correct information. The particle size is finer with the higher impact sphere velocity. Based on the property, Re numbers of the jetting flow of each case were calculated. The conclusion could be found that even the impact velocity is higher; the flow situation is relatively more close to the laminar flow. This factor might be supportive to explain situation that the lower turbulence intensity of case 3 and case 4.
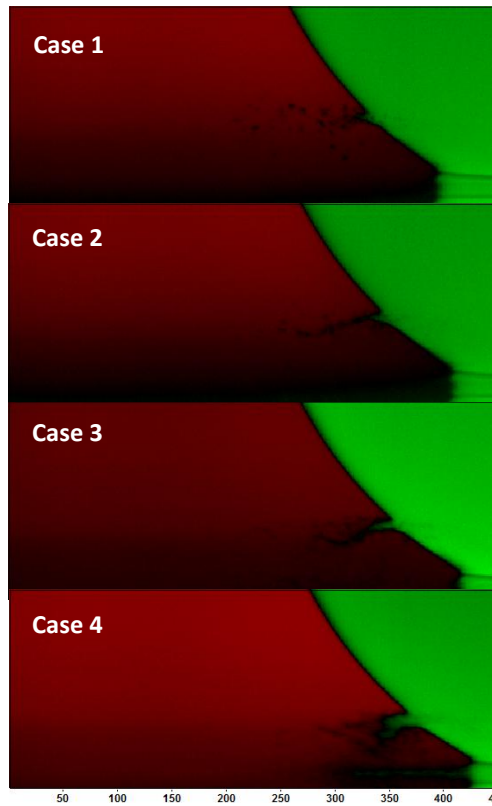
Figure 30. t/T = 0.044 of 4 cases. Close view of jetting particles. The unit of scale is pixel and 1 pixel = 0.2 (mm).

Figure 30 shows a series of randomly selected images of four cases and the images are passed an intensive constricted color-scale process in order to have a clearer view of jetting particles.

The diameter of jetting particles in case 1 is about 5 pixels which is 1 mm and the jetting particles are large enough to be observed in case 1. The size of jetting particles in case 2 is slightly finer than 5 pixels, which is around 4 pixels. The particle size is even finer in the case 3 and the particles are not easily distinguished. However, we found that

the diameter of particles is about 1 pixel by carefully inspecting the images. The jetting

particles size in case 4 are not visually observed, and the particle size is defined as

around 0.1mm. The Reynolds numbers are calculated with jetting water particle size and

are summarized in table 4.

Table 4. Reynolds numbers of jetting flow

Case #	Jetting water particle size (mm)	Re
Case 1	1	10714
Case 2	0.8	9285
Case 3	0.2	4107
Case 4	0.1	2410

       The finger-like shape of jetting flow can be clearly observed in case 3 and case 4.

The appearance also learned by Thoroddsen et al. (2004). Maximum Reynolds number

for case 1 of jetting flow is about 4 times higher of case 4.

       The relationship between the normalized maximum jetting speed and Reynolds

number referred to the contacting sphere diameter for each case is showed in Fig. 31.

The dash-line in the figure was brought out by Thoroddsen et al. (2004). They concluded

that the jetting speed has a positive relationship with the impacting Reynolds number.

For our study, the range of Reynolds numbers is about $3\times10^4 \sim 1.5\times10^5$. The Reynolds numbers are referred to the contacting diameter of sphere corresponding the moment of maximum jetting speed occurred. However, our results are against the analytical solution derived by Thoroddesn et al. (2004), and the possible reason is the difference of Reynolds number. Three differences are observed .First, the wide range of Reynolds numbers for Thoroddsen (dash line) is around $2.5\times10^3 \sim 4\times10^5$. Secondly, the Reynolds numbers they defined were based on the entire diameter of experimental sphere. Finally, various impact sphere speeds and the different viscosity of liquids were applied for their experiments, resulting in the widespread range of Reynolds numbers. The liquid used for this study was water to maintain the same fluid viscosity for 4 cases.

The relationship of the diameter of sphere and the contacting diameter which is corresponding to the occurrence of maximum jetting velocity and the occurrence of the initial jetting velocity was illustrated in Fig. 32. The explanation of each symbol is as following. Square: the identical zone Star: the opposite zone. Black: D_c is the contact diameter of maximum speed occurred. Red: D_c is the contact diameter of initial jetting speed detected.

The initial jetting detected between $D_c/D = 0.2 \sim 0.3$, which D is the diameter of sphere, is shown as the red symbols.. The black symbols present the max jetting occurred. A positive tendency is observed as the linear relationship of Reynolds numbers and D_c/D. Reynolds number is greatly proportional to the ratio of D_c to D.

69

After normalizing D$_c$, the results are still in opposite to Thoroddsen's results (solid line). The reasons might be the narrower range of our Reynolds number compared with Thoroddsen et al. (2004) and the same kind of liquid though out the entire experiments. In this circumstance, the impacting sphere Reynolds number might play a role to affect the moments of jetting emerged.

However, Thoroddsen et al., (2004) stated that the higher viscosity with the same impact velocity caused to the higher ratio of D_c/D. This conclusion supported our measurements that the higher Re number with the lager ration of D_c/D.
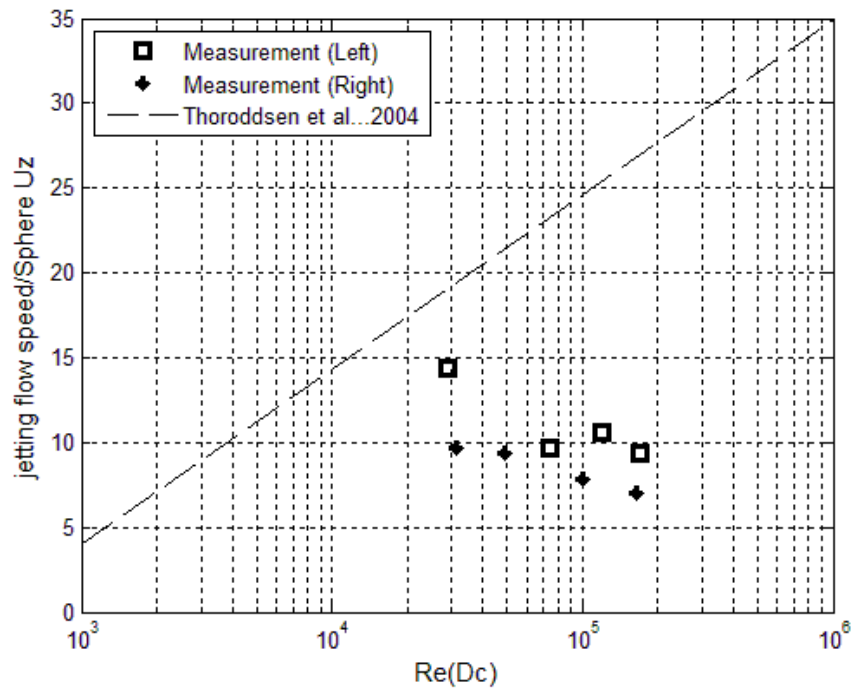
Figure 31. Normalized max jetting flow speed versus the impacting Reynolds mumbles.
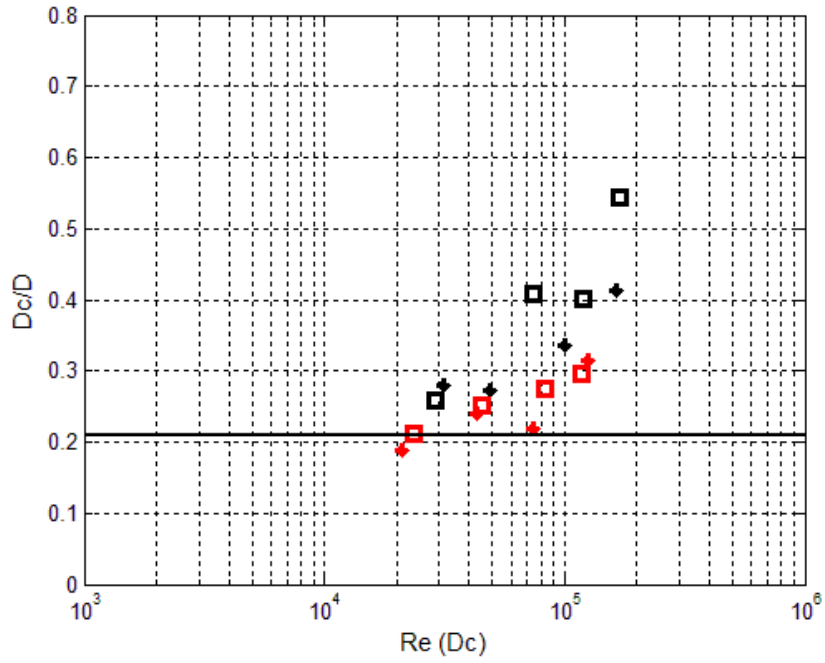
Figure 32. Red: initial jetting flow detected. Black: maximum jetting flow speed occurred.
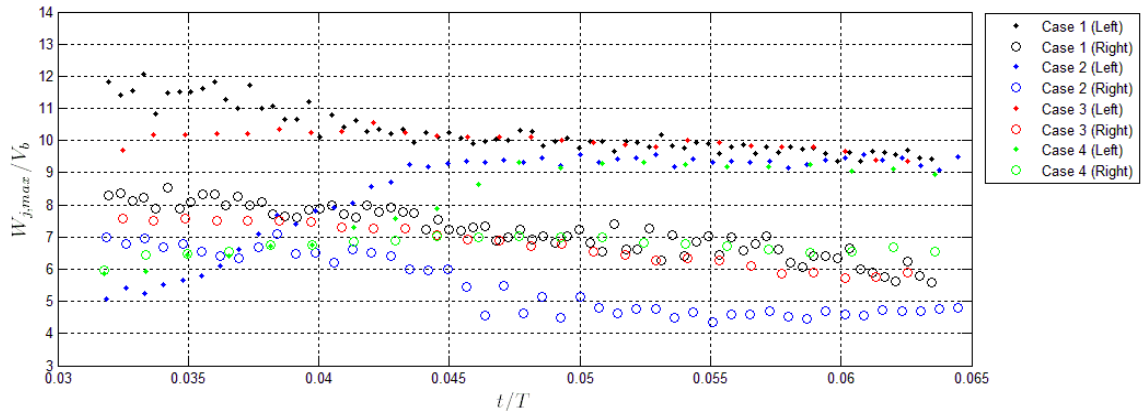
Figure 33. Normalized maximum jetting speed. V_b: sphere vertical impacting velocity, $W_{jetting}$: maximum jetting flow speed.

71

The relationship between normalized time-series max jetting speed and the impacting vertical sphere velocity is shown in Fig. 33. The normalized maximum jetting speed is defined as $V_b/W_{j,max}$. Vb stands for the vertical impacting velocity of sphere, and $W_{j,max}$ is the maximum jetting flow speed. The solid dots are the slamming measurements in the identical zone and the circles are gained from the opposite zone. These normalized time-series results show a good convergence within four cases. For the identical zone, the maximum jetting speeds converged to about 9~10, although the initial ratio is different in 4 cases. For the opposite zone, the maximum jetting speed converged to about 5~7 and it is about 2/3 of $V_b/W_{j,max}$ in the identical zone.

The normalized jetting speed is decreased over time in both identical and opposite zones. The results provide the evidence that the normalized jetting speed may not be different at a narrow range of Reynolds number with the same viscosity of experimental fluid and the ratio even more converged eventually.

CHAPTER V

CORRELATION OF JETTING FLOW AND SLAMMING PRESSURE

Mass Balance

Figure 34 shows the relationship of normalized time series impact pressures and maximum jetting speeds. The control volume considering the mass conservation of in the system is applied to calculate the mass balance, shown in Fig. 35.The mass flux and momentum flux are not taken in to account in the right and left boundaries of control volume based on the assumption that the boundaries are infinite. The calculation of mass flux and momentum flux are based on the equation (5) to (8).

$$\frac{DM_{sys}}{Dt} = \frac{\partial}{\partial t}\int_{CV}\rho dV + \int_{CS}\rho\vec{V}\cdot\hat{n}dA = 0 \tag{5}$$

$$\frac{\partial}{\partial t}\int_{CV}\rho dV = \rho A_{water-sphere}\frac{\partial\delta}{\partial t} \tag{6}$$

$$-\frac{\partial\delta}{\partial t} = U_{sphere} \tag{7}$$

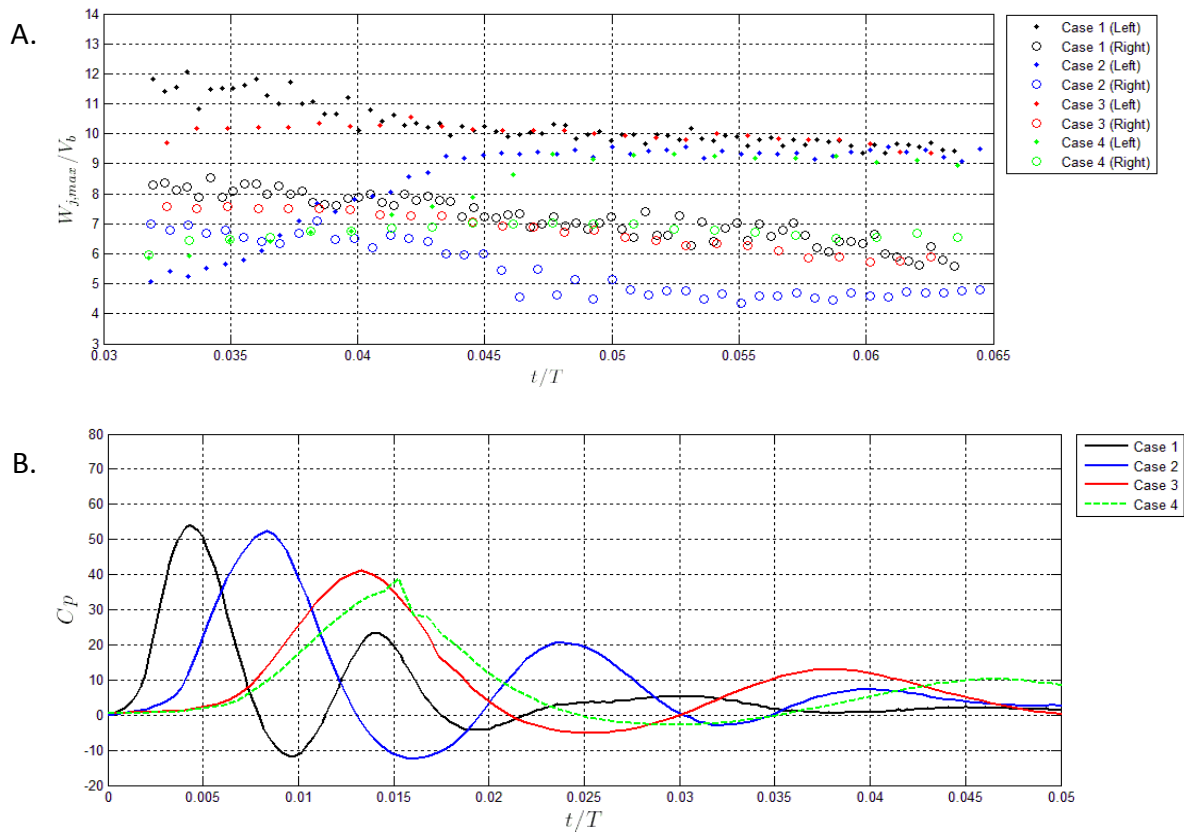$$\dot{m}_{jetting} + \dot{m}_{pool} = \dot{m}_{deformation} \tag{8}$$

Figure 34. (A) Normalized maximum jetting flow speeds among 4 cases. (B) Non-dimensional time-series pressure records at the 0 degree measuring point.
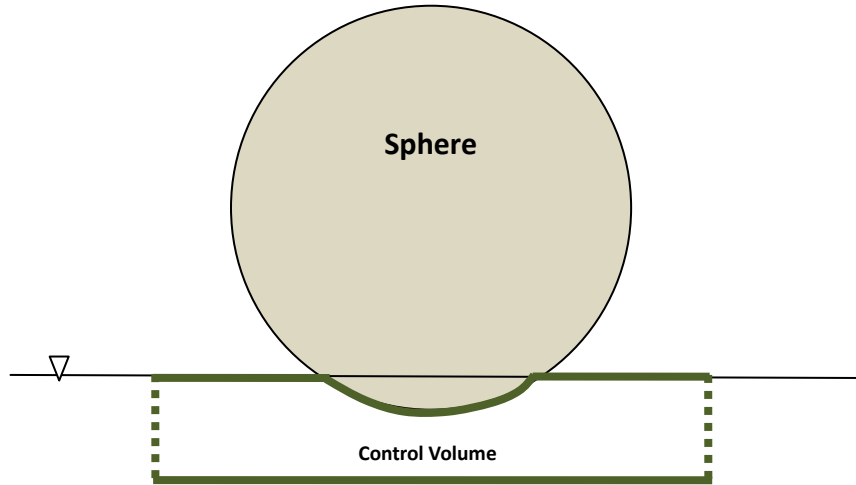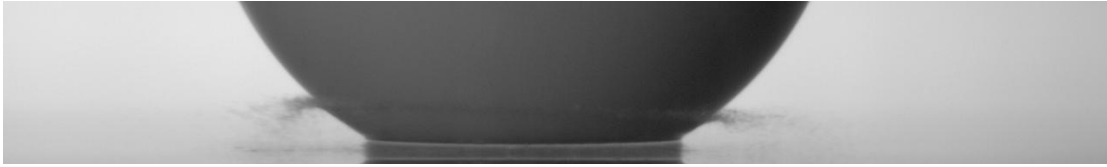
Figure 35. Raw experimental image at 0.0025 (s) after sphere impacting and control volume for calculating mass balance and momentum balance for the system.

The mass flow rate of deformation was brought out as $\dot{m}_{deformation} = \int_{cs} \rho \vec{V} \cdot \hat{n} dA$,

and where $\vec{V}$ is the sphere impacting velocity which is vertical to the sphere surface as described in Fig. 36. In order to consider the total force of the system in x-direction motion of sphere in the identical zone and the opposite zone, the mass flow rates were calculated separately and listing in Fig. 36.

The particular time and case selected for the following calculation is 0.0025 s and Case 4 after sphere impacting which is the time of maximum jetting speed occurred. At the moment of maximum jetting flow speed occurred t = 0.0025 s, the sphere moved forward along with the symmetry axis about 0.724 cm under the water surface and the angle of the wet surface is 25.23°. Since the sphere velocity (vertical to water surface) over the wet surface from $+25.23^{\circ} \sim -25.23^{\circ}$ is as a function of $\sin\theta$, the mass flow rate can be restated as $\dot{m}_{deformation} = \rho R \iint_{cs} V(\sin\theta) d(\sin\theta) dy$, where R is the radius of sphere, $V(\sin\theta) = -1.14462(\sin\theta)^2 + 3.1319(\sin\theta) + 2.9126$ (m/s), and the width is assumed as the unit length, 1 cm, for the Y-direction integration.
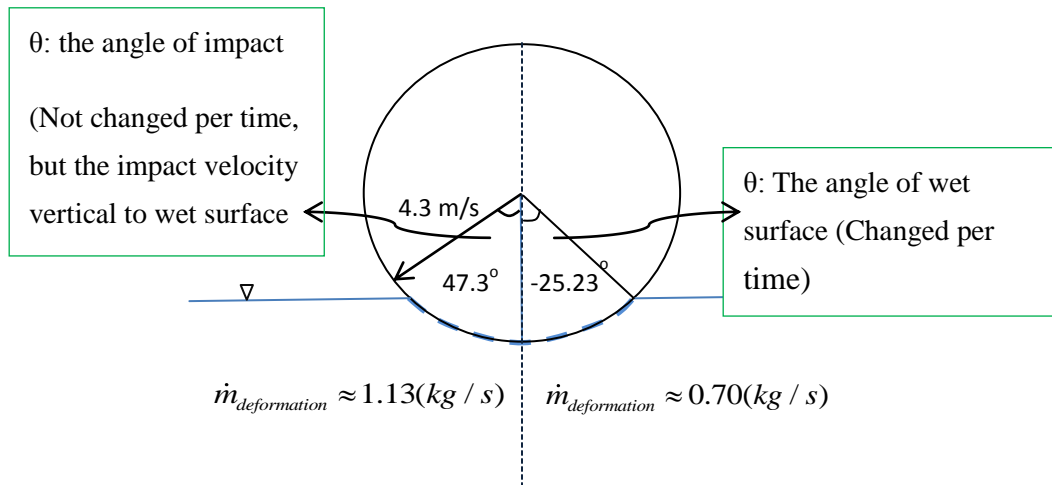
Figure 36. Deformation of the mass flow rates (identical zone and opposite zone), impacting sphere velocity and the angle of wet surface at the time frame = 0.0025(s) of case 4.

Mass flow rates of deformation of control volume are about 1.13 *kg/s* in the identical zone and 0.70 *kg/s* in the opposite zone. The mass flow rate of jetting is then considered. However, the area of jetting spilled out is difficultly observed by the raw experimental images, so100% of the mass flow rate came from the deformation transferred to the jetting was assumed for the next section.

Momentum Balance

Momentum balance between impacting force and jetting flow at the same time frame is calculated through the information of mass balance. The measured pressures at

the five points around the sphere surface and jetting flow speed are employed to examine the momentum balance of the control volume which is identical to one in mass balance.

The pressure regression profiles around sphere according to the measured peak pressures at five different measuring points are as the sine function of impacting angle. The total force around the contacting surface at the moment of the maximum jetting speed occurred is:

$$F = \iint P dx dy$$, where the impacting pressure, P, is as the sine function of impact angles. The calculation of force is redefined as: $F = \iint PRd(\sin\theta)dy$, where R is the radius of the sphere. The width, 1 cm, was assumed as the unit length for the Y-direction integration. Because of the different physical situations and different conditions of peak pressures in the opposite and identical zones separately according to the x-dir motion of sphree, the calculations of monmentum conservation were conducted separately as well.

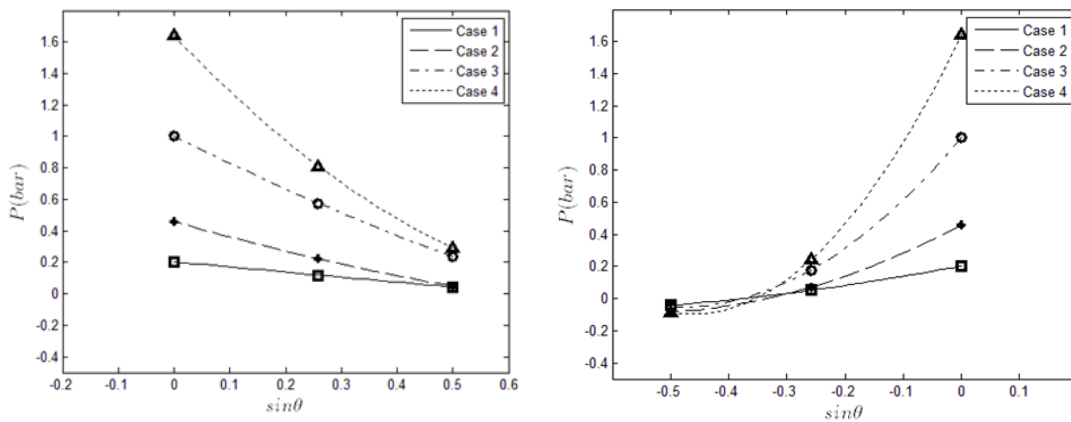**Figure 37.** Correlation of measured peak pressures versus impacting angle (sinθ).

The impact angles were defined related to the locations of sensors as mentioned in the chapter III

$$P_{identical} = \frac{1}{2}\rho V_b^2 \left(50.33(\sin\theta)^2 - 90.01(\sin\theta) + 39.42\right)(\text{pa}). \qquad (9)$$

$$P_{opposite} = \frac{1}{2}\rho V_b^2 \left(195.53(\sin\theta)^2 + 180.64(\sin\theta) + 39.42\right)(\text{pa}). \qquad (10)$$

The hehaviors of pressures in the opposite zone and identical zone are different. The regression curve were fitted separately in the two zones. The above equations (9) and (10) are demonstrated for case 4 only. Where V_b is the sphere vertical velocity 2.9 m/s and ρ is the density of fluid.

The impacting force is calculated as $F_X = P \times \sin\theta \cdot dA$ and $F_Z = P \times \cos\theta \cdot dA$ in order to discuss the force balance between sphere impacting and resulted jetting flow, where θ, the angle of wet surface, is measured between the sphere impacting depth and the sphere radius. At this particular time frame $t = 0.0025$ s and $\theta = 25.23^o$ and -25.23^o, $F_X = 6.49(N)$ and $F_Z = 30.79(N)$ in the identical zone, and $F_X = -2.06(N)$ and $F_Z = 17.14(N)$ in the opposite zone.

Base on the equation: $F_{jetting} = \int_{cs} V\rho\vec{V} \cdot \hat{n} dA = V_{max-jetting}\dot{m}_{jetting}$ (x-direction). The jetting flow velocity is about 27.00 m/sin the identical zone and is around 20.34 m/s in the opposite zone. The total force of the jetting in the identical zone is 30.57 N. The the total measured force of the opposite zone is about 14.24 N. Where $\dot{m}_{jetting} = \dot{m}_{deformation}$ is adopted. One important asumption is that the density for calculating the mass flow rate is used as 1000 kg/m^3.

Based on the linear momentum balance, an assumption for the impacting force of z-direction acting inside the control volume is that the source offering the spilling out of the jetting flow was adopted. On the other hand, the jetting flows initially spill along the z-direction. However they may be suddenly reflected by the surface of the sphere and may change their moving direction or immediately climb up along the sphere surface. Jetting flow then leaves the sphere surface when the surface tension does not play an important role. The x-direction of impacting force may cause that the mass inside the pool flow out toward to the outside zone of the control volume, and this situation may lead to the loss of mass. The further understanding is necessary to explore in the future. The total jetting force is about 44.81 N and the impacting force in z-direction is 47.93 N.

Time-series momentum balance is taken into consideration because the impacting force is as the function of wetted surface angle. Jetting forces in each wet surface angle could also be determined because of the present measured time-series maximum jetting flow speed. The impacting forces in z-direction and jetting forces are displayed as the red line and blue dots in Fig. 38, respectively.
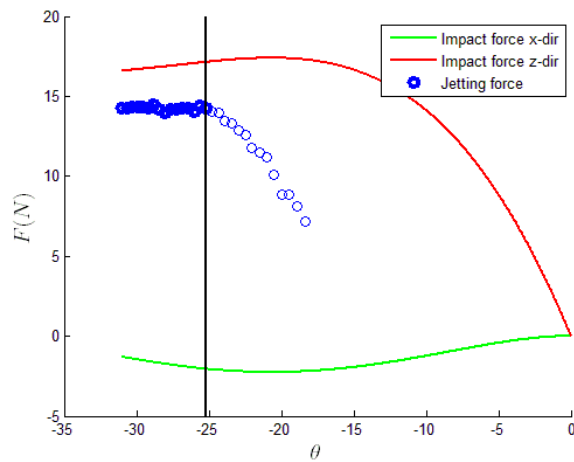
Identical zone:
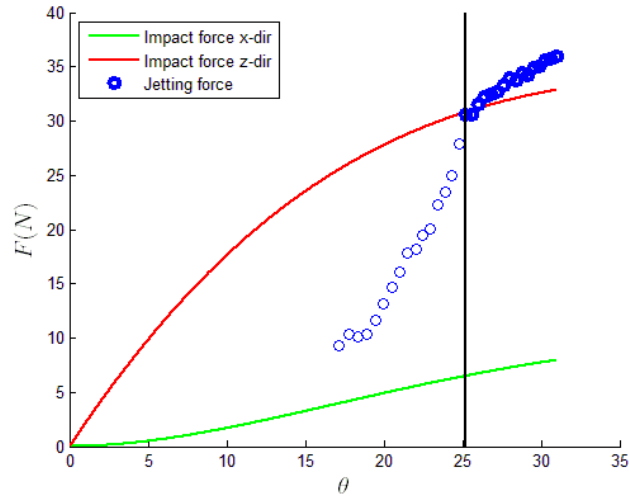
Opposite zone:

Figure 38. Series of impact forces and jetting flow forces through the increasing of angle of wet surface. The solid black lines indicate the moment of maximum jetting flow velocity occurred.

When the moment of maximum jetting flow speeds occurs at +25.23°, the impacting force in z direction matches with the jetting flow force in the identical zone, shown in Fig. 38. However, in the opposite zone, the jetting flow force is underestimated about 20% of the impact force in z direction at -25.23°. The reason may be the energy absorbed by the pool or underestimated jetting flow speed in the opposite zone.

Between the wet surface angle of 25.23° and -25.23°, the jetting flow force is much lower than the impacting force in z direction. The possible reason is that the frame rate of high speed camera, 12000 fps, is not sufficient to catch the jetting flow speed before measured maximum jetting flow speed comes out.

If 100% of force F_{impact} (in z direction) which is came from the sphere impacting transferring to the jetting force is assumed, the maximum jetting flow velocity can be expressed as $U_{jetting} = F_{impact}/\dot{m}_{jetting}$,where $\dot{m}_{jetting}$ is the mass flow rate of the jetting, which is assumed as the same with the mass flow rate of deformation of control volume. The calculated maximum jetting flow speed and measured jetting flow speed are illustrated separately in the identical zone and opposite zone, shown in Fig. 39.

Identical zone:
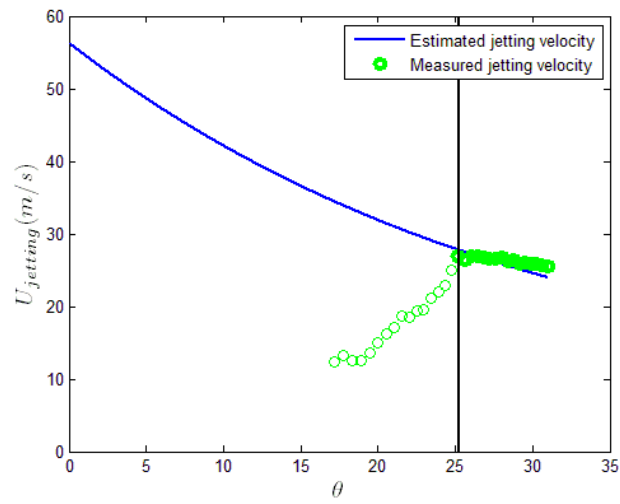
Opposite zone:
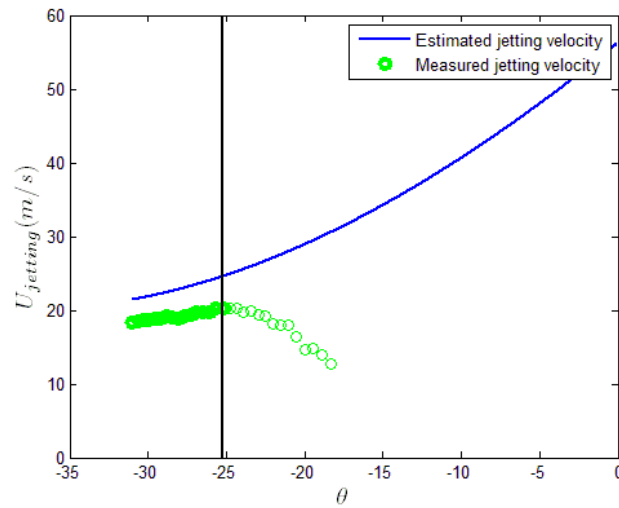
Figure 39. The measured jetting flow velocity and estimated jetting flow velocity at various impacting angle.

The estimated maximum jetting flow velocity is calculated after the sphere impacting. The estimated maximum jetting flow velocity at 0° is about 57 m/s, and it is almost 20 times larger than the vertical sphere impacting velocity. The result is more close to the estimation of Thoroddsen et al. (2004). From their results, the ratio of jetting flow velocity to vertical impacting velocity is about 30 when the impact Re considering the whole diameter of sphere is around $2.5 \sim 3.0 \times 10^5$.

The maximum jetting flow velocities start to be converged from about the wet surface of 25° in the identical zone. Meanwhile, although the jetting flow speed is still undervalued in the opposite zone, it start to be close to estimated jetting flow speed when the wet surface angle is smaller than -25°.

The estimations of thickness of the area for jetting flow spilling out were also conducted in Fig. 40. The thickness of jetting spilling area is the function as $\dot{m}_{jetting} = \rho U_{jetting} A$, where $U_{jetting}$ is measured jetting flow velocity and the unit length, 1 cm, in y-direction of spilling out area was assumed. Where A is the area of jetting flow passed through and ρ is the density of fluid. The area of jetting flow spilled out can be evaluated also based on the assumption that 100% mass flow transferred from $\dot{m}_{deformation}$ to $\dot{m}_{jetting}$.
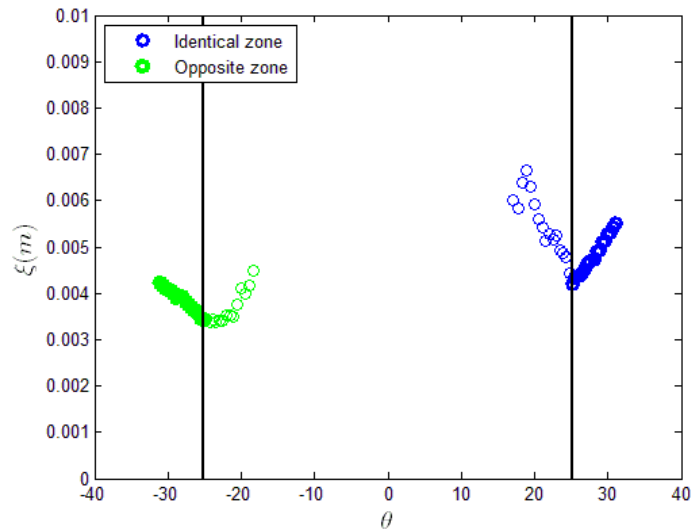
Figure 40. Evaluated thicknesses of jetting spilling areas.

The black solid lines indicate the moment of occurrence for the maximum jetting flow speed at 25.23° and -25.23°. There are two types of tendencies of both identical zone and opposite zone. Based on the previous discussion that the measured jetting speed may be underestimated because of the insufficient frame rate of high speed camera, the evaluated thickness between $-25.23^{\circ} \sim 25.23^{\circ}$ of the wet surface angle may be useless. However, the estimated thickness of jetting flow spilling out between 25.23° and -25.23° may be a big picture to understand the physical mechanism of jetting.

CHAPTER VI

CONCLUSIONS

The objective of our study is to figure out the correlation of force transferred from the impacting to the jetting flow. The experimental approach is used to investigate the relationship of the impacting and the jetting flow.

In order to understand the pressure profile over wet surface of the sphere and corresponding jetting flow field, four sphere impacting speed conditions are conducted in the hydro lab for five designed impact angles

Time-series impacting pressures were successfully carried out by pressure sensor which is inserted inside the sphere during entire experimental procedure. BIV approach was also employed to study the jetting flow filed. A high speed camera was used to obtain the experimental images for the BIV calculation.

The information of pressure measurements and jetting flow fields are able to be combined to find out the momentum balance within the entire system. Both the impact forces and the jetting forces were evaluated successfully. The jetting flow speeds were also estimated through the jetting forces.

The conclusions are as following:

1. For each case with five measuring impact angles, the highest peak pressures among five angles were always found at the 0° impact angle. A particular positive peak value can be observed in every impact angle except -30°. Only negative pressures were found at this particular measured point for all cases.

2. Down-zero crossing pressures happened only after the first peak of pressures detected at the 0° impact angle in each case. In the impact angle of 0°, the pressures were gradually converged to zero during 0.02 s time period of observations. The obvious oscillations for pressures were also found at this angle. The second peak of pressure at this stage was around one to fourth of the pressure of first peak.

3. At the measuring points 15° and 30°, after the peak values occurred, the pressures were gradually depressed but never converged to zero during the 0.02 (s) time period. Especially at 30° measured point, the pressures stayed about half of the maximum peak. At the measuring point -15°, the pressures rose first to the maximum peak and then oscillated, and went down to cross zero point pressure and kept negative values.

4. The rising time of peak pressure was also discussed. The rising time was less than 0.2 ms for the first peak and is about 0.4 ms for the second peak at the 0° measuring point.

5. Overall, the patterns of pressures for each different measuring point were quite different, such as the peak pressures, the rising time of peak pressures and the oscillation situations. However, the tendencies of all cases at any particular measuring points were quite similar.

6. The comparisons between the theoretical pressure coefficient and experimental pressure coefficient were also carried out. At the 0° impact angle, the time-series pressure coefficients were compared. The theoretical pressure coefficient was

87

similar with experimental one when the impacting speed was higher. The differences of the peak pressures estimated for case 1 to case 4 were as 40%, 14%, 13% and 5%, respectively. Generally, the theoretical pressure coefficients are higher than the experimental values.

7. The comparison between the theory and experimental peak pressures were also conducted for 15° and 30° impact angles. At the impact angle of 30°, the theoretical pressure has no difference with experimental pressure. However, the theoretical peak pressures were overestimated especially when the impact sphere speed went higher at 15° impact angle. After considering the surface area of pressure sensor for the calculation of impact angle, the experimental peak pressures matched the peak pressures derived from the theory by using the impact angle equal to 18.76^o which is corresponding to the upper boundary of pressure sensor.

8. For the jetting flow field measurements, the jetting flow speeds and moving directions were also obtained for all cases, and presented as velocity vectors and contours with six selected normalized time frames in the Chapter IV. The vectors and contours were acquired from the average of 20 repeated measurements for each case. Generally, the maximum jetting speeds didn't detect right reading immediately after the sphere impacting. They were detected around 0.003~0.005 s after the sphere initially contacted water surface. The decelerated situations occurred right after the maximum jetting speeds happened. The maximum jesting flow speed in the identical zone for each case is about 10 to 12 times larger than

the sphere vertical impacting velocity.

9. The normalized turbulence intensities of entire jetting flow fields were also carried out. The turbulence intensities were higher when the impacting sphere speed is lower and corresponding Re number of jetting particles is higher.

10. The path-line of maximum jetting flow detected was also drawn for each case. The locations of maximum jetting speed were always found in the front of flow fields.   The pattern of the path-line is quite similar in the identical zone but very different in the opposite zone. Drag force may be the factor to cause the situation. The further study is necessary for the fully understanding.

11. Maximum jetting flow speeds in each identical and opposite zone were recorded for each time frames. For the identical zone, the normalized jetting flow speeds gradually converged to 9~10 at 0.06 time factor. However, the tendency was not found in the opposite zone.

12. Control volume approach was introduced for considering the momentum balance of the slamming system. Before the moment of the maximum jetting flow speed was able to find out, the force of jetting was below the impacting force.

13. Maximum jetting flow speed was also evaluated. The maximum jetting flow speed was depressed with the increasing of angle of wet surface. Like the situation for calculating force balance between impacting and jetting, the measured jetting velocities significantly matched the evaluated jetting velocities after the moment of maximum jetting speed detected. The initial evaluated jetting velocity is around 18 times higher than the vertical impacting velocity. Similar

results were found in Thoroddsen et al. (2004).

REFERENCES

Abraham, J., J. Gorman, F. Reseghetti, E. Sparrow, J. Stark, and T. Shepard (2014), Modeling and numerical simulation of the forces acting on a sphere during early-water entry, Ocean Engineering, 76, 1-9.

Battistin, D., and A. Iafrati (2003), Hydrodynamic loads during water entry of two-dimensional and axisymmetric bodies, Journal of Fluids and Structures, 17, 643-664.

Chang, K.-A., K. Ariyarathne, and R. Mercier (2011), Three-dimensional green water velocity on a model structure, Experiments in Fluids, 51, 327-345.

De Backer, G., M. Vantorre, C. Beels, J. De Pré, S. Victor, J. De Rouck, C. Blommaert, and W. Van Paepegem (2009), Experimental investigation of water impact on axisymmetric bodies, Applied Ocean Research, 31, 143-156.

Faltinsen, O. M., M. Landrini, and M. Greco (2004), Slamming in marine applications, Journal of Engineering Mathematics, 48, 187-217.

Gu, H. B., L. Qian, D. M. Causon, C. G. Mingham, and P. Lin (2014), Numerical simulation of water impact of solid bodies with vertical and oblique entries, Ocean Engineering, 75, 128-137.

Huera-Huarte, F. J., D. Jeon, and M. Gharib (2011), Experimental investigation of water slamming loads on panels, Ocean Engineering, 38, 1347-1355.

Jepsen, R. A., S. S. Yoon, and B. Demosthenous (2006), Effects of air on splashing

during a droplet impact, paper presented at Proceedings 19rd International Conference on Liquid Atomization and Spray Systems, Toronto, Canada.

Lin, M.-C., and L.-D. Shieh (1997), Flow visualization and pressure characteristics of a cylinder for water impact, Applied Ocean Research, 19, 101-112 .

Maruzewski, P., D. L. Touzé, G. Oger, and F. Avellan (2010), SPH high-performance computing simulations of rigid solids impacting the free-surface of water, Journal of Hydraulic Research, 48, 126-134.

Moghisi, M., and P. T. Squire (1981), An experimental investigation of the initial force of impact on a sphere striking a liquid surface, Journal of Fluid Mechanics, 108, 133-146

Ryu, Y., K.-A. Chang, and H.-J. Lim (2005), Use of bubble image velocimetry for measurement of plunging wave impinging on structure and associated greenwater, Measurement Science and Technology, 16, 1945-1953.

Ryu, Y., K.-A. Chang, and R. Mercier (2007a), Application of dam-break flow to green water prediction, Applied Ocean Research, 29, 128-136.

Ryu, Y., K.-A. Chang, and R. Mercier (2007b), Runup and green water velocities due to breaking wave impinging and overtopping, Experiments in Fluids, 43, 555-567.

Song, Y. K., K.-A. Chang, Y. Ryu, and S. H. Kwon (2013), Experimental study on flow kinematics and impact pressure in liquid sloshing, Experiments in Fluids, 54, 1592-1611.

Thoroddsen, S. T., T. G. Etoh, K. Takehara, and Y. Takano (2004), Impact jetting by a solid sphere, Journal of Fluid Mechanics, 499, 139-148

Van Nuffel, D., K. S. Vepa, I. De Baere, P. Lava, M. Kersemans, J. Degrieck, J. De Rouck, and W. Van Paepegem (2013), A comparison between the experimental and theoretical impact pressures acting on a horizontal quasi-rigid cylinder during vertical water entry, Ocean Engineering, 77, 42-54.

Yoon, S. S., R. A. Jepsen, M. R. Nissen, and T. J. O'Hern (2007), Experimental investigation o splashing and nonlinear fingerlike instability of large water drops, Journal of Fluids and Structures, 23, 101-115.